Acta Materialia 311 (2026) 122210

Contents lists available at ScienceDirect

Acta Materialia

journal homepage: www.elsevier.com/locate/actamat

Full length article

Role of boron in yield strength softening and plastic deformation mechanisms in an equiatomic TiNbZrHfTa refractory high-entropy alloy

Chengguang Wu [a], Shaolou Wei [a,*], Loïc Perrière [b], Jean-Philippe Couzinié [b], Dirk Ponge [a], Yan Ma [a,c,*], Dierk Raabe [a,*]

[a] Max Planck Institute for Sustainable Materials, Max-Planck-Straße 1, 40237 Düsseldorf, Germany
[b] Univ Paris Est Creteil, CNRS, ICMPE, UMR 7182, 2 rue Henri Dunant, 94320 Thiais, France
[c] Department of Materials Science and Engineering, Delft University of Technology, Mekelweg 2, 2628 CD Delft, the Netherlands

ARTICLE INFO

Keywords:
Refractory high-entropy alloys
Boron segregation
Grain boundary chemistry
Yield strength softening
Grain boundary strain localization

ABSTRACT

Grain boundary (GB) engineering is an effective tool for improving the mechanical properties of metallic materials. In this study, we added 30 appm boron (B) to an equiatomic TiNbZrHfTa refractory high-entropy alloy (HEA), and found that the GB chemistry has been altered. B preferentially segregates to GBs with the co-segregation of Zr and depletion of Nb and Ta, as revealed by atom probe tomography probing. This change in GB chemistry affects the macroscopic load-bearing performance of the HEA, where a reduction in the yield strength by ~6.2 ± 0.7% is observed, *i.e.*, 869.8 ± 10.4 MPa of the B-doped HEA *vs.* 920.7 ± 3.7 MPa of the B-free HEA. Additionally, a correlation between GB chemistry and the plastic deformation at GBs is found, indicated by changes in the crystallographic slip traces and the Luster-Morris compatibility factor among adjacent crystals. More specifically, we find that (i) B-decorated GBs accommodate higher adjacent plastic strain levels, which is manifested as an out-of-plane offset (via GB shear localization) between two neighboring grains; and (ii) in the B-doped case, slip transfer across GBs requires a lower misalignment between slip planes or slip directions as compared with the B-free sample. This study thus enhances our understanding of the role of GB chemistry in the mechanical properties of polycrystalline body-centered cubic HEAs, leveraging opportunities for GB segregation engineering in this field.

1. Introduction

Refractory high-entropy alloys (HEAs) composed of multiple principal elements (four or more) offer advantages over dilute alloys in improving mechanical and functional properties due to the quasi-infinite compositional space, which allows for tweaking microstructures and their interplay with chemistry [1–3]. Although their high Peierls barrier contributes to the intrinsic high strength of these refractory HEAs (*e.g.*, ~1200 MPa for TiNbZrHfTa), most of them exhibit low room-temperature (RT) ductility (~10% and less), making potential applications of these alloys challenging [4–7]. This limitation is also evident in the small difference between ultimate tensile strength and the strength for initiating cleavage fracture, which arises from the presence of less densely packed atomic planes in body-centered cubic (BCC) alloys [8,9]. This fact means that most refractory HEAs are more likely to fail in a brittle manner before significant plastic deformation can take place. Their tensile ductility usually does not exceed 10%, and most researchers therefore probe ductility under compression [6,10–14]. The low RT formability also makes it difficult to eliminate defects from casting in refractory HEAs, such as porosity, microcracks, dendritic microstructure inhomogeneities, and Scheil-segregation-related elemental variations that can trigger material failure [5,15]. Therefore, the design of refractory HEAs with enhanced RT formability at maintained high strength remains a challenge in this field.

Significant efforts, including reducing grain size, designing heterogeneous microstructures, or introducing the transformation-induced plasticity (TRIP) effect, have been employed to improve the ductility of these alloys [15–17]. These mechanisms contribute to enhanced work hardening capacity, thus increasing ductility. Nevertheless, some of these approaches, particularly TRIP, work only for metastable alloys with specific alloy compositions [18,19]. An alternative strategy for improving the ductility of refractory HEAs is grain boundary (GB) segregation engineering, altering interface properties by atomic-scale compositional tuning of the GB decoration state [20–22]. As derived

* Corresponding authors.
E-mail addresses: sl.wei@mpi-susmat.de (S. Wei), yan.ma@tudelft.nl (Y. Ma), d.raabe@mpi-susmat.de (D. Raabe).

https://doi.org/10.1016/j.actamat.2026.122210
Received 8 December 2025; Received in revised form 11 March 2026; Accepted 31 March 2026
Available online 6 April 2026

from classical thermodynamics in terms of the interface isotherm, solutes preferentially reside at GBs driven by the reduction in Gibbs free energy [23–25]. Among several conceivable dopants, the metalloid element boron (B) has garnered significant attention for its ability to enhance both the strength and ductility of polycrystalline materials. Its effectiveness even at ppm-level concentrations makes it a cost-efficient alternative to more costly alloying elements [26–31]. For example, the addition of 400 appm B in an as-cast NbMoTaW solid solution resulted in mitigating oxygen contamination at GBs, thereby alleviating room-temperature brittleness [28]. Additionally, enhanced GB drag and reduced Gibbs-Thompson forces caused by B segregation can reduce grain coarsening during the heat exposure of polycrystalline refractory HEAs [27,29].

Here, we report on a counterintuitive phenomenon observed in a 30 appm B-doped equiatomic TiNbZrHfTa refractory HEA, where yield strength softening (reduction by ~6.2 ± 0.7%, from 920.7 ± 3.7 MPa to 869.8 ± 10.4 MPa) is observed, despite grain refinement being achieved by introducing B to GBs. To explore the underlying mechanisms for this unexpected softening behavior, site-specific atom probe tomography (APT) was conducted to measure the GB chemistry upon B doping. The associated plastic deformation behavior was further evaluated using electron backscatter diffraction (EBSD) and scanning electron microscopy (SEM), along with crystallographic analysis and quantitative assessments of micro-deformation events near the GBs. From these experiments, we find that: (1) B addition significantly alters the GB chemistry, with B and Zr appearing as co-segregants; (2) the moderate reduction in yield strength is mainly due to a lower Hall-Petch coefficient caused by segregation of B as well as Zr at GBs, compromising strengthening that would have been otherwise expected by grain refinement; (3) GB regions tend to accommodate higher strain upon B doping than B-free material; and (4) the inception of slip transfer can be mitigated by GB strain localization, where active slip transfer is significantly confined to lower misalignments for both slip planes and directions when B segregation is present.

2. Experimental methods

2.1. Materials

The equimolar TiNbZrHfTa refractory HEAs with and without the addition of 0.003 at.% (30 appm) B were cast using arc-melting under Ar atmosphere. Pure metals (>99.95 wt.%) were used to synthesize the base alloy. B doping was conducted by adding high-purity TiB_2. The as-cast samples were cold-rolled to a total thickness reduction of 80%, followed by recrystallization annealing into the BCC solid solution regime at 1100 °C for 5 h under continuous helium flow. The annealed materials were quenched in helium atmosphere by withdrawing the furnace while keeping the samples inside the silica tube. The B concentration was determined to be 5 appm and 31 appm by the Inductively Coupled Plasma-Mass Spectrometer (ICP-MS). This subtle contamination of B in the B-free specimen is primarily attributed to the metallurgical impurity initially present in the raw materials. Hereafter, the TiNbZrHfTa HEAs with the addition of 0 appm B and 30 appm B were denoted as B-free and B-doped specimens, respectively. We also note that the overall oxygen content of the specimens was below 0.40 at.% as measured by atom probed tomography (APT), a value not expected to alter the mechanical properties of the material [32].

2.2. Microstructure characterization

The metallographic specimens were ground from 220 grit up to 4000 grit SiC sandpapers and subsequently polished with 50 nm colloidal silica oxide particle suspension to obtain a mirror-finished surface. A combination of secondary electron, backscatter electron imaging, energy-dispersive X-ray spectroscopy (EDS), and electron backscatter diffraction (EBSD) techniques was used for microstructure characterization (Zeiss Sigma 500, Germany). The EBSD scans were carried out at an acceleration energy of 15 kV and a current of 5 nA, at a scanning step size of 1.0 μm. Post-processing of the EBSD data and the extraction of the crystallographic information for theoretical analysis were done using the commercial OIM software (version 8.0). Surface slip trace analysis and slip transfer quantification were carried out using a home-built STrCryst software package (https://github.com/shaolouwei/STrCryst).

To quantitatively explore the effect of GB chemistry on plastic deformation, we conducted analysis of crystallographic orientation data and slip line morphology to determine the activated slip modes by slip trace analysis. This technique has been applied before in the investigation of deformation mechanisms for both single- and dual-phase metallic alloys [33–35]. However, three potential sources of inaccuracies should be mentioned: (1) slip trace observation and the associated shear quantification is influenced by surface quality; (2) identification of slip variants is complicated due to the curvature of the slip traces, especially in regions with high and heterogeneous local strains; and (3) the present work primarily focuses on slip configurations at the meso-scale (*i.e.*, grain size scale), while more complex {112} plus {123} composite slip plane modes might become discernable at the nanoscopic scale [36–39]. To mitigate potential artifacts, the specimens were tilted to ±10° to validate the occurrence of discrete crystallographically aligned slip steps prior to imaging. Considering the geometric relation between the crystal orientations and slip lines, the active slip modes can be calculated via the following equation,

$$\mathbf{t} = \left(g^{-1}\cdot\mathbf{n}\right) \times \mathbf{N} \tag{1}$$

where **t** represents the unit directional vector corresponding to the slip plane. **n**, and **N** are the unit outer normal directions of the slip plane (crystal frame) and sample surface (sample frame), respectively. g denotes the orthogonal normalized coordinate transformation matrix, *i.e.*, the local crystal orientation [40],

$$g = \begin{bmatrix} \cos\varphi_1\cos\varphi_2 - \sin\varphi_1\sin\varphi_2\cos\Phi & \sin\varphi_1\cos\varphi_2 + \cos\varphi_1\sin\varphi_2\cos\Phi & \sin\varphi_2\sin\Phi \\ -\cos\varphi_1\sin\varphi_2 - \sin\varphi_1\cos\varphi_2\cos\Phi & -\sin\varphi_1\sin\varphi_2 + \cos\varphi_1\cos\varphi_2\cos\Phi & \cos\varphi_2\sin\Phi \\ \sin\varphi_1\sin\Phi & -\cos\varphi_1\sin\Phi & \cos\Phi \end{bmatrix} \tag{2}$$

where (φ_1, Φ, φ_2) are the Euler angles following Bunge's convention, which can be obtained from the EBSD measurements [40]. For slip trace analysis, $\{110\}\langle 1\bar{1}1\rangle$, $\{112\}\langle 11\bar{1}\rangle$, and $\{123\}\langle 11\bar{1}\rangle$ slip systems are all taken into consideration due to the similar packing density of the {110}, {112}, and {123} planes in a BCC crystal structure [37]. The angle (φ) between the slip line and the loading axis can then be calculated via,

$$\varphi = \arccos\left|\frac{\mathbf{t}\cdot\mathbf{f}}{|\mathbf{t}|\cdot|\mathbf{f}|}\right| \tag{3}$$

In this equation, $\mathbf{f} = [010]^{\mathrm{T}}$, denotes the far-field uniaxial loading direction. Theoretical slip traces are determined by applying a ±10° ($\Delta\varphi$) deviation tolerance as compared with the experimental

observations. The corresponding Schmid factors (m) specific to the activated slip systems are calculated through [41],

$$m = [(g\cdot\mathbf{f})\cdot\mathbf{n}]\cdot[(g\cdot\mathbf{f})\cdot\mathbf{s}] \quad (4)$$

Here, **n** and **s** represent the unit slip plane normal and the unit slip direction, respectively.

Synchrotron high-energy X-ray diffraction (HEXRD) experiments were conducted in a transmission mode at the Powder Diffraction and Total Scattering Beamline P02.1 of PETRA III at Deutsches Elektronen-Synchrotron (DESY) in Hamburg, Germany [42]. A beam with a fixed energy of 60 keV was employed to obtain a monochromatic X-ray with a wavelength of ~0.207 Å. The acquired diffraction peaks were integrated and subsequently post-analyzed using GSAS-II software [43]. Based on the XRD line broadening, the Williamson-Hall method was used to evaluate the dislocation density (ρ) in the specimens [44]:

$$\beta\cos\theta = 4\varepsilon\sin\theta + \frac{k\lambda}{D} \quad (5)$$

where β was the full width of half maximum (FWHM) of the diffraction peak at θ. ε, λ, and D represent the microstrain, the wavelength of the X-ray beam, and the crystallite size, respectively. k is a constant for different materials, where 0.94 is usually used for BCC-type alloys [45]. Then, the dislocation density was calculated according to [46]:

$$\rho = \frac{2\sqrt{3}\varepsilon}{D|b|} \quad (6)$$

where b was the magnitude of the Burgers vector.

Atom probe tomography (APT) was employed to analyze the local chemistry at GBs down to near-atomic resolution. The APT tips were prepared using the site-specific lift-out method with the aid of the EBSD technique (to identify GBs prior to lift-out) using an FEI Helios NanoLab 660i dual-beam SEM/FIB instrument. The APT measurements were conducted in a LEAP 5000XR instrument, operated in reflectron mode, to ensure high mass resolution. Laser mode APT probing was employed for the measurements, using a tip temperature, laser energy, pulse rate, and detection rate of 70 K, 60 pJ, 100 kHz, and 0.5% (5 ions per 10,000 pulses), respectively. The reconstruction and post-analysis of APT data were carried out using the AP suite software (version 6.1).

2.3. Uniaxial tensile testing

Rectangular dog bone-shaped tensile specimens with a gauge geometry of 4.0 × 2.0 × 1.0 mm^3 were prepared using electrical discharge machining. The specimens were ground with SiC sandpapers (from 200 grit to 4000 grit), followed by fine-polishing with 50 nm colloidal silica oxide particle suspension before tensile tests. A Kammrath and Weiss stress rig (strain rate: 1.25 × 10^{-3} s^{-1}) equipped with an optical camera (every 1 s) for digital image correlation (DIC) analysis was employed for the tensile test. A virtual extensometer (speckle patterns) was adopted to measure the local strains, and the data were processed using the Aramis GOM Correlate 2020 software (V6.3.0, GOM GmbH). Three tests were repeated for each microstructural condition.

3. Results

3.1. Microstructure and grain boundary segregation upon B doping

Both B-free and B-doped TiNbZrHfTa refractory HEAs exhibit an equiaxed grain microstructure (Figs. 1a and b), showing a near-random orientation distribution, *i.e.*, with negligible crystallographic texture (**Fig. S1**). High-angle GBs (> 75%) constitute the major type of GBs in both specimens. The grain sizes of B-free and B-doped specimens are 69.9 ± 27.2 μm and 53.9 ± 23.5 μm, respectively (inserts in Figs. 1a and b). Grain refinement is observed in case of B addition, which will be discussed in detail in Section 4.1. The corresponding EDS elemental distribution maps across the magnified regions marked in Figs. 1a and b show a homogeneous distribution of all elements. Additionally, the compositions for the B-free and B-doped specimens are determined to be $Ti_{19.77}Nb_{18.75}Zr_{21.27}Hf_{20.70}Ta_{19.51}$ and $Ti_{19.21}Nb_{18.74}Zr_{20.66}Hf_{20.86}Ta_{20.52}$ (in at.%), respectively (**Table S1**), consistent with the nominal equiatomic composition.

The HEXRD profiles confirm that (Fig. 2a) both specimens reveal a single-phase microstructure with body-centered cubic (BCC) crystal structure. It is worth noting that no diffraction peaks of a boride phase are observed in the B-doped specimen. The lattice parameters are 3.399 Å and 3.396 Å (**Fig. S2**) for the B-free and B-doped specimens, respectively. From the linear fitting curves of $\beta\cos\theta$ as a function of $4\sin\theta$ (Fig. 2b), the microstrain (ε) and crystalline size (D) can be extracted from the slopes and intercepts, respectively, to calculate the dislocation density (Eqs. (5) and (6)). As revealed in Fig. 2c, both specimens possess a similar level of the initial dislocation density, *i.e.*, 1.72 × 10^{14} m^{-2} and

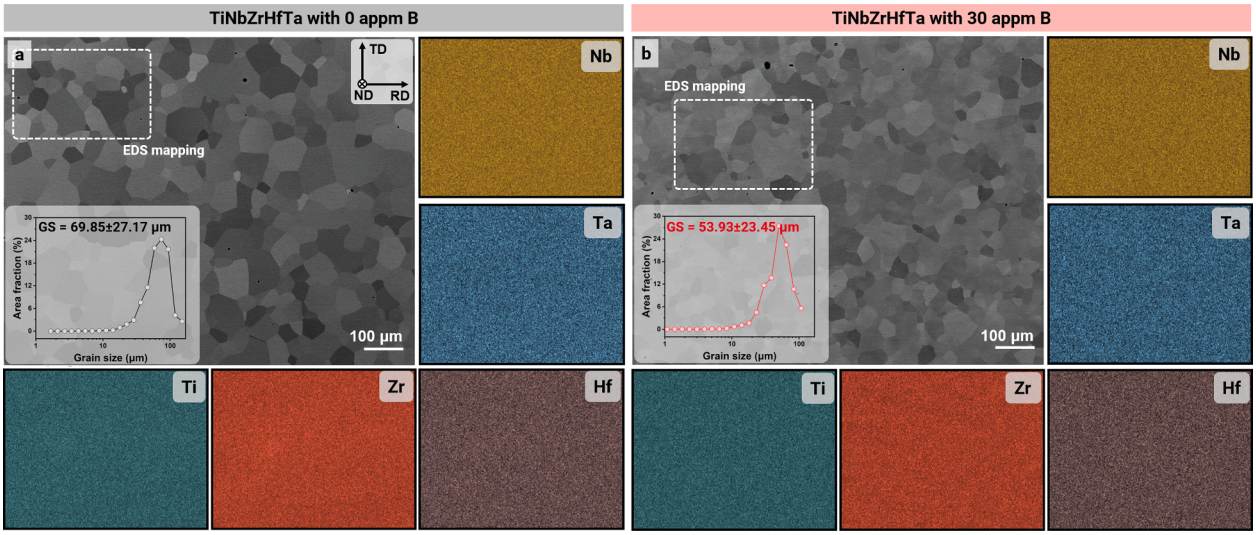

Fig. 1. Representative scanning electron microscopy (SEM) images of the (a) B-free and (b) B-doped TiNbZrHfTa HEAs, and their corresponding energy-dispersive X-ray spectroscopy (EDS) mapping of individual principal elements. The regions for EDS mapping are indicated by white dashed lines. The inserts represent the grain size distribution obtained over 50 grains from (a) and (b), respectively. TD, ND, and RD represent transverse, normal, and rolling directions, respectively.

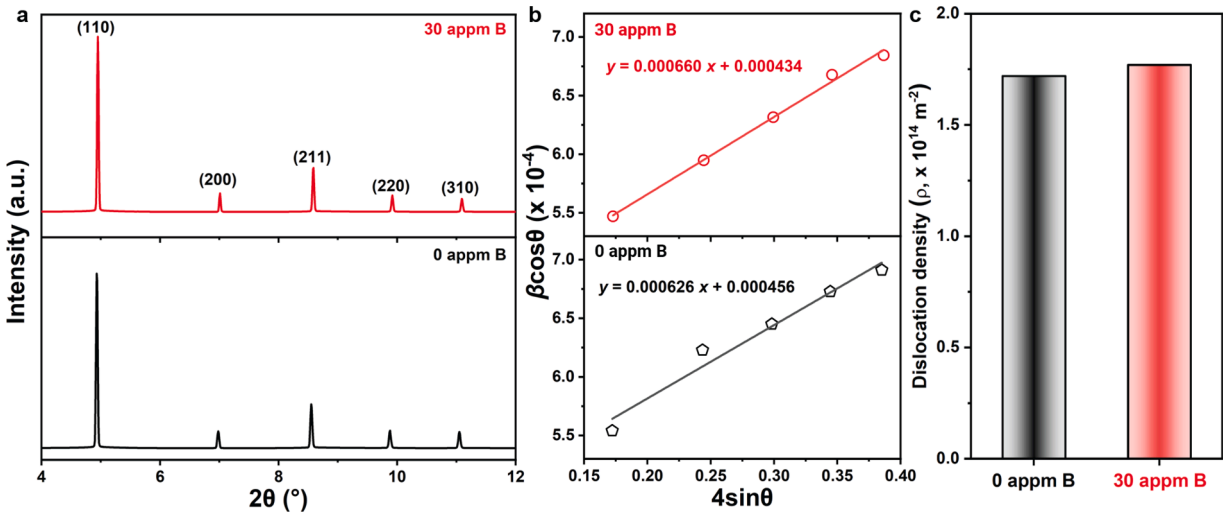

Fig. 2. (a) Synchrotron high-energy X-ray diffraction (HEXRD) profiles of the TiNbZrHfTa HEAs without and with 30 appm B. (b) Plots of $\beta\cos\theta$ versus $4\sin\theta$ and their corresponding linear-fitted curves. β represents the full width of half maximum (FWHM) while θ is the diffraction angle. (c) Calculated dislocation density of the TiNbZrHfTa HEAs without and with 30 appm B doping.

1.77×10^{14} m^{-2} in the B-free and B-doped specimens, respectively. These relatively high dislocation densities observed after recrystallization is mainly attributed to the low self- and solute-diffusivities of refractory elements and strong solute-dislocation interactions in HEAs, which impede dislocation cross slip and annihilation [6,47–49]. These results suggest that the small addition of B (30 appm) leads to a grain

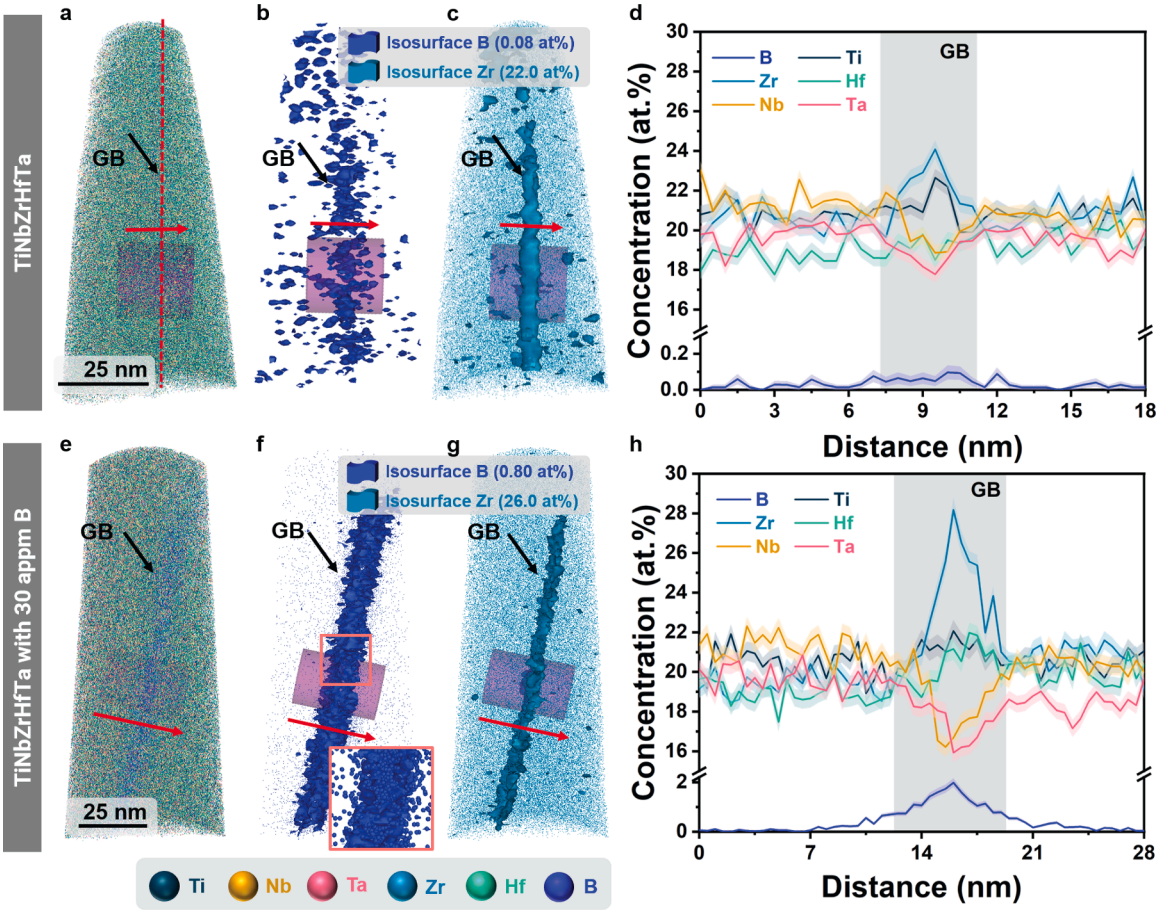

Fig. 3. Atom probe tomography (APT) analysis for the grain boundary of TiNbZrHfTa HEAs with (a-d) 0 appm B and (e-h) 30 appm B. Grain boundaries are indicated by black arrows. B atomic distribution (in blue) with a 0.08 at.% and 0.80 at.% B isosurface for TiNbZrHfTa HEAs containing (b) 0 appm B and (f) 30 appm B, respectively. Insert in (f) shows the enrichment of B atoms (depicted in spheres) within the grain boundary. 1D concentration profiles of B, Ti, Zr, Hf, Nb, and Ta across the grain boundary of the TiNbZrHfTa HEAs containing (d) 0 appm B and (h) 30 appm B as highlighted with purple cylinders with a diameter of 25 nm. Red arrows indicate the direction of the cylinders.

refinement but does not cause obvious changes in other microstructure features, such as grain morphology, phase constituent, chemistry at the microscopic scale, and initial dislocation density.

Although the observed grain refinement signifies potential segregation of B at GBs, it remains crucial to identify the actual distribution of B in the specimens. B is known to preferably decorate GBs, driven by the reduction of their free energy according to the Gibbs adsorption theorem [27,29]. Three-dimensional APT analysis was therefore employed to quantitatively investigate the GB chemistry of both specimens (Figs. 3 and **S3**). The misorientations of the probed GBs are determined to be 44.57° and 47.10° using EBSD for the B-free and B-doped specimens (**Fig. S4**), respectively. The GBs in APT datasets are identified by the decoration of B atoms (marked by blue dots). The B-free specimen exhibits a slight enrichment of B (max. 0.10 at.%) at the GB, as highlighted by the isoconcentration surface of B (0.08 at.%, Fig. 3b). The metallurgical impurity initially present in the raw materials mainly contributes to this subtle contamination, consistent with the ICP-MS result. Additionally, co-segregation of Zr at the GB is detected up to 24.08 at.%, as shown by the isoconcentration surface containing 22.00 at.% Zr, in contrast to its bulk concentration in the matrix, *i.e.*, 20.77 at.%. Slight depletion of Nb and Ta (Figs. 3c and d) by 1.92 at.% and 1.52 at.% from the equiatomic composition is also observed at the GB, as shown in the 1D concentration profiles. The lowest mixing enthalpy between B and Zr (−71 kJ/mol) predominantly contributes to such a co-segregation behavior compared to its interaction with the other principal bulk elements [50]. In contrast, the depletion of Nb and Ta is mainly ascribed to their high mixing enthalpy with B (both values are −54 kJ/mol) [50]. In the B-doped specimen, the quantity of B at GBs is much more pronounced as highlighted by a set of isosurfaces delineating regions containing more than 0.80 at.% B (Fig. 3f). An enrichment of up to 1.98 at.% B is found at the GB, whereas the concentration of B in the matrix is below 0.10 at.% (Fig. 3h), demonstrating that B is indeed trapped at the GBs. Similar to the B-free specimen, co-segregation of Zr at the GB is observed in the B-doped specimen (Fig. 3*g*), but with a much higher concentration, reaching up to 28.20 at.% (Fig. 3h). Additionally, depletion of Nb and Ta is observed with a stronger extent (a reduction of 3.27 at.% and 3.36 at.% for Nb and Ta, respectively). These differences in GB chemistry between the B-free and B-doped TiNbZrHfTa HEAs can significantly affect not only the microstructure (*e.g.*, grain refinement) but also the mechanical response of the materials, particularly those associated with GB properties (GB strengthening, GB strain localization, slip transfer across the GB, *etc.*). These aspects will be elaborated further in the **Discussion** section.

3.2. Tensile properties of alloy variant with addition of B

Fig. 4a presents the uniaxial tensile properties of the TiNbZrHfTa refractory HEAs without and with B addition (using three repeated flat tensile tests). The B-free specimen plastically yields at 920.7 ± 3.7 MPa, followed by a modest strain hardening process, reaching an ultimate tensile strength of 940.4 ± 15.2 MPa at a uniform elongation of 3.80%. In contrast, a lower yield strength of 869.8 ± 10.4 MPa is observed for the B-doped specimens (insert in Fig. 4a), with a reduction by 6.2 ± 0.7% compared with the B-free specimens. As B addition in other alloys often results in an enhancement in strength [26,29,30], such yield strength softening by B addition as found here for the B-doped TiNbZrHfTa alloy necessitates a more fundamental understanding of the underlying mechanism, which will be discussed in Section 4.1. Both alloys exhibit a similar level of total elongation (22.2 ± 0.2% and 20.9 ± 1.1% for B-free and B-doped specimens, respectively), and strain-hardening rates (Fig. 4b).

3.3. Slip trace analysis

Figs. 5a and b show two regions of interest that underwent deformation via multiple slip and cross slip in the B-doped specimen. In addition, predominant single slip regions also occurred inside the grains (**Fig. S5**). The determination of different slip activities was conducted using fast-Fourier transform patterns, and the corresponding details are revealed in **Fig. S6**. In the multiple slip example, two types of straight slip traces (with different Burgers vectors) were found with an intersecting angle of 45.66°. These two slip traces were identified to be the $(121)[1\bar{1}1]$ (m = 0.381) and $(2\bar{3}1)[111]$ (m = 0.326) slip systems, as revealed when comparing the observed slip traces with the calculated ones (Fig. 5a). For the cases shown in Fig. 5b, curved slip traces (with the same Burgers vector) were identified, corresponding to the activated $(12\bar{3})[\bar{1}11]$ (m = 0.468) and $(1\bar{1}2)[\bar{1}11]$ (m = 0.448) slip systems. This transition between active slip planes is indicative of cross-slip, which is one characteristic feature of slip activity in BCC systems [8]. It is important to note that cross-slip in BCC systems often manifests itself in the form of continuous and frequent slip-plane alternation or pencil glide, distinct from classical discrete cross-slip events typically observed in face-centered cubic (FCC) crystals [8,39,51,52]. In addition to the slip activities in the grains, the presence of GB strain localization was observed as an out-of-plane offset between adjacent grains (*e.g.*, G1 and G2 in Figs. 5c, **S5,** and **S7**). In this case, plasticity is accommodated by GB strain localization. A sharp increase in gray value in the secondary electron image (by ~101) is detected across the GB region (Fig. 5d).

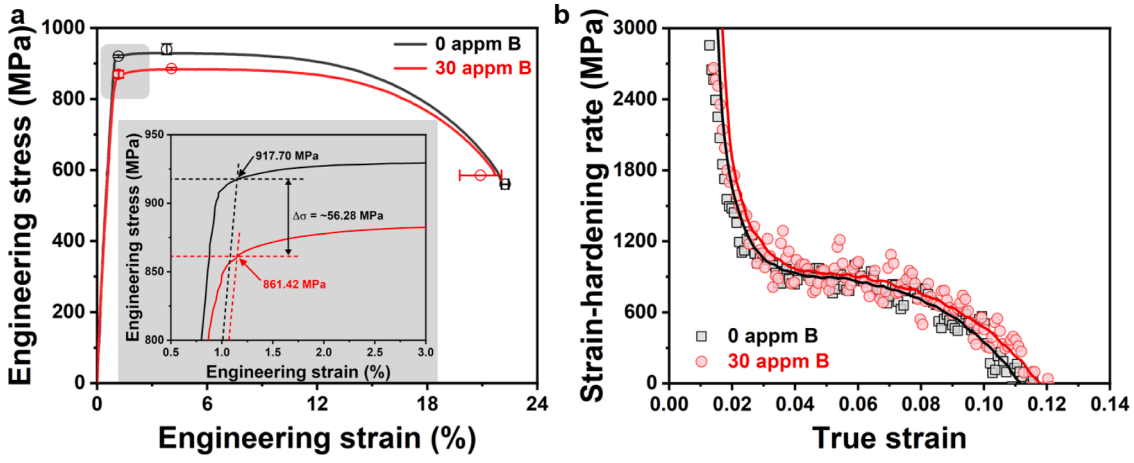

Fig. 4. (a) Engineering stress-strain curves of the TiNbZrHfTa HEAs without and with the addition of B at 30 appm. The mean values (shown as open circles) and corresponding error bars are obtained over three repeated tests. Insert is the enlarged view of the strain range from 0.5% to 3.0%, revealing the yield strength softening in the specimen with the addition of 30 appm B. (b) Strain-hardening rates as a function of true strain.

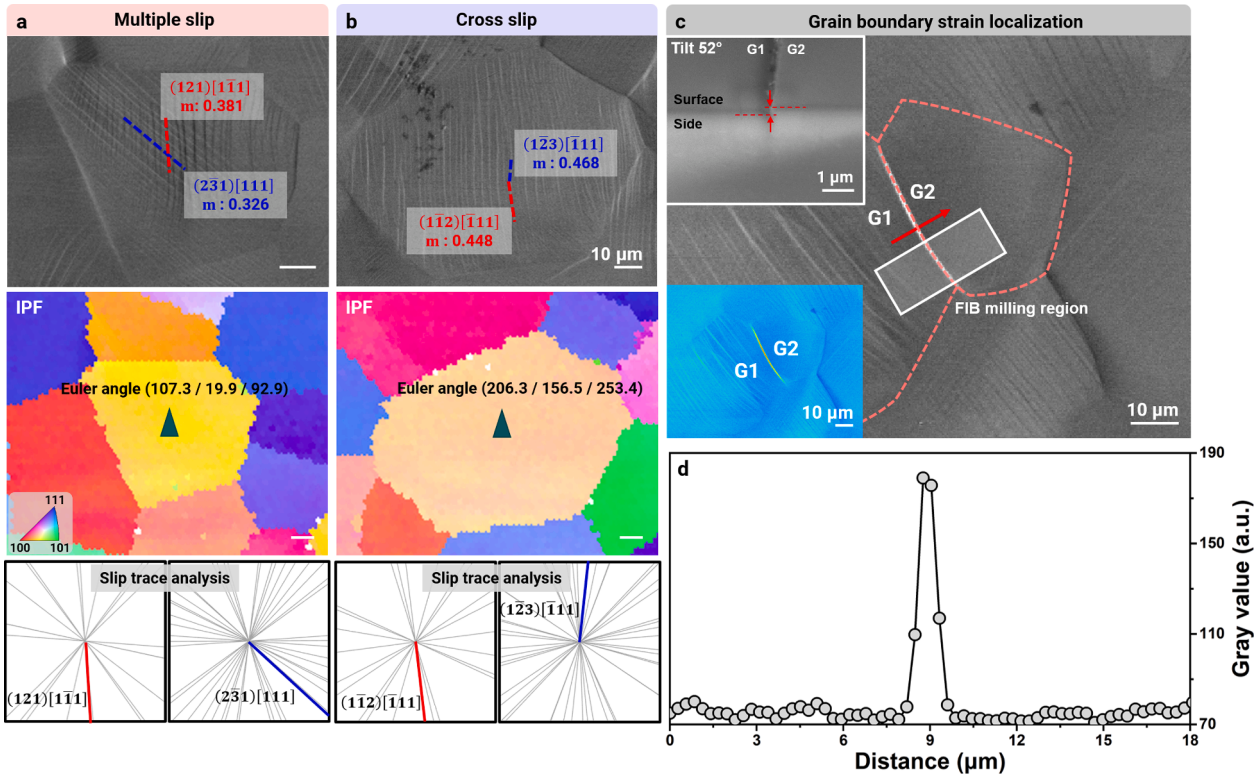

Fig. 5. Representative B-doped grains at a global strain of 2% with (a) multiple-slip activity and (b) cross-slip activity and the corresponding inverse pole figure (IPF) maps as well as the slip trace analysis for identifying the operating slip systems, respectively. (c) Observation of grain boundary strain localization acquired at an incident plastic deformation (2% strain). The top insert in (c) is the SEM image of the cross-sectional view of the grain couple with a tilt angle of 52°, showing the height misfit between the adjacent two grains (marked with G1 and G2). The bottom insert in (c) is the post-processed SEM image with a color transform using a blue lookup table, revealing the sharp increase in contrast at the grain boundary region. (d) The gray values across the grain boundary as highlighted by a red arrow in (c). All the SEM micrographs have been post-processed with a brightness increase of +20% and a contrast increase of +20% to enhance feature visibility.

Therefore, we adopted the first derivative of gray value (the absolute value above 20) as an indicator to identify the strain localization at the GB instead of milling all the GBs for side-view observations (**Fig. S8**) for quantitative assessments on the deformation modes accommodating plasticity.

4. Discussion

4.1. Competing effects between Hall-Petch coefficient (K_y) and grain size (d) on the change in yield strength

A decrease in yield strength was observed in the B-doped specimen compared with the B-free reference material (Fig. 4a). This yield strength softening behavior seems contradictory to many earlier observations on the simultaneous increase in both yield strength and ductility found in other metallic materials with B addition, *e.g.*, steels, Ti-based alloys and metal matrix composite [26,29–31]. Generally, in a linear mean-field approximation, yield strength (σ_{ys}) of metallic alloys can be expressed as follows [53],

$$\sigma_{ys} = \sigma_{gb} + \sigma_{dislo} + \sigma_{P} + \sigma_{ss} \tag{7}$$

where σ_{gb}, σ_{dislo}, σ_{P}, and σ_{ss} denote the strengthening effects from GBs, dislocations, precipitates, and solid solution, respectively. In this study, changes in the σ_{dislo} (similar dislocation densities in the initial state, Fig. 2c), σ_{P} (no formation of secondary phases, Fig. 2a), and σ_{ss} (similar alloy composition as well as the appm-level addition of B, **Fig. S9**) are not affected upon B doping. Therefore, the decrease in yield strength in the sample with B addition is mainly ascribed to the contribution from GBs (σ_{gb}). This hypothesis also aligns with the experimental observations that the major differences in microstructure in these two specimens are the grain size and the elemental segregation at GBs (Figs. 1 and 3). The strengthening effect from GBs can be expressed by the phenomenological Hall-Petch relationship [54–56],

$$\sigma_{gb} = K_y/\sqrt{d} \tag{8}$$

where K_y is a material-dependent constant, referred to as GB resistance or GB strength coefficient, while d is the mean grain size. These two factors will be discussed in detail individually to explore the plausible mechanisms causing the yield strength softening.

4.1.1. Grain refinement

In the B-doped HEA, the grain size d is reduced due to the GB segregation of B and Zr, which promotes solute drag effects and alters the effective driving pressure (P) for grain growth compared with the B-free alloy [27,29,57]. The driving pressure for grain growth originates from the reduction in stored energy associated with GBs as the grain size increases. Assuming a uniform stored energy and isotropic distribution of the driving pressure, it can be approximated as: $P = \frac{\alpha\gamma_s}{R}$, where α, γ_s, and R represent the shape factor, boundary energy, and grain radius, respectively [57]. The segregation of B and Zr to the interfaces reduces γ_s, thus lowering the effective driving pressure and resulting in grain refinement [57–59].

In addition, this grain refinement behavior can also be captured within the framework of the classical mean-field grain growth kinetics [27],

$$D_t^n - D_0^n = C \times t \tag{9}$$

where D_t, D_0, and n are the measured mean grain size at annealing time t, initial grain size (assumed to be 1 μm [27]), and kinetic exponent

quantifying the grain growth behavior, respectively. C represents the kinetic constant and is expressed in Arrhenius form as $C = C_0 \times \exp(-Q/RT)$ [60], where C_0, Q, R, and T denote the pre-exponential factor, activation energy for grain growth, gas constant and annealing temperature, respectively. Then, we obtain,

$$\ln\left\{\left(D_f^n - D_0^n\right)/t\right\} = \ln C_0 - (Q/RT) \tag{10}$$

The kinetic exponent n generally ranges from 2 (for uniform grain growth) to 4 (indicating the abnormal grain growth) [61]. Here, $n = 3$ is selected for the calculation considering the broad grain size distribution (Fig. 1) in the investigated HEAs. With $n = 3$, $D_f = \frac{9}{8}D_t$ can be obtained, representing the final grain size [62,63]. Therefore, the apparent activation energies for grain growth (Q) are calculated to be approximately 273.2 kJ/mol, and 282.0 kJ/mol for the B-free and B-doped HEAs, respectively. The addition of B (and the associated Zr co-segregation) leads to an increase in Q (Fig. 6a), thus resulting in the reduction in grain size d, which is consistent with the grain refinement observed after B doping (Fig. 1). From the mechanical point of view, however, a yield strength softening was revealed in the B-doped HEA, suggesting potential changes in GB chemistry and its effects on the constant K_y of the Hall-Petch relationship (Eq. (8)). Such effects will be discussed in more detail in the next section.

4.1.2. *The effect of grain boundary chemistry on K_y*

The effect of B segregation as well as the associated alternation in GB chemistry can be demonstrated based on the selection of plastic yielding models, for example, the pile-up and the GB ledge models. In the pile-up model, yielding is propagated when the stress concentration is generated by the dislocation pile-up in one grain, activating dislocations in the adjacent grain. In another scenario (GB ledge model), ledges (*i.e.*, atomic-scale steps) at GBs can also act as dislocation sources. In the current investigation, the emission of dislocations and the formation of dislocation channels are observed in the vicinity of the GB at an early stage of plastic deformation (at a global strain of around 1.2%) without plasticity being detected in the grain interior, see **Fig. S10**. These differences underpin that GBs play a key role in yielding and may serve as dislocation sources in the B-doped HEAs [64]. Along this hypothesis, we assume activation of the GB ledge mode for GB-related dislocation production, and K_y can then be expressed as

$$K_y = \alpha M G^{\mathrm{GB}} b\sqrt{3m} \tag{11}$$

where α, M, G^{GB}, b, and m represent a material-dependent constant, Taylor factor, shear modulus of the GB, the magnitude of the Burgers vector, and the ledge density, respectively. The EBSD maps (**Fig. S1**) suggest that the types of the GBs are similar for the B-free and B-doped HEAs, with high-angle GBs accounting for more than 75%. The GB ledge density, which is a function of the misorientation angle [65], is thereby assumed to be identical for these two cases. It is worth noting that this simplification based on the statistically similar distributions of low- and high-angle GBs carries inherent uncertainty into the quantitative deconvolution of the Hall-Petch coefficient, as it neglects the possible atomic-scale changes at GBs induced by solute segregation (*i.e.*, the co-segregation of B and Zr). Such segregation behavior can alter local features, such as ledge density, local disorder, and excess free volume, without affecting the crystalline macroscopic misorientation [21, 66–68]. These atomic-scale modifications could, in turn, influence the effective density of dislocation nucleation sites at GBs. Direct atomic-scale structural characterization of these specific GBs is required to quantify such segregation-induced structural changes and the resulting effective ledge density, which is beyond the scope of this work.

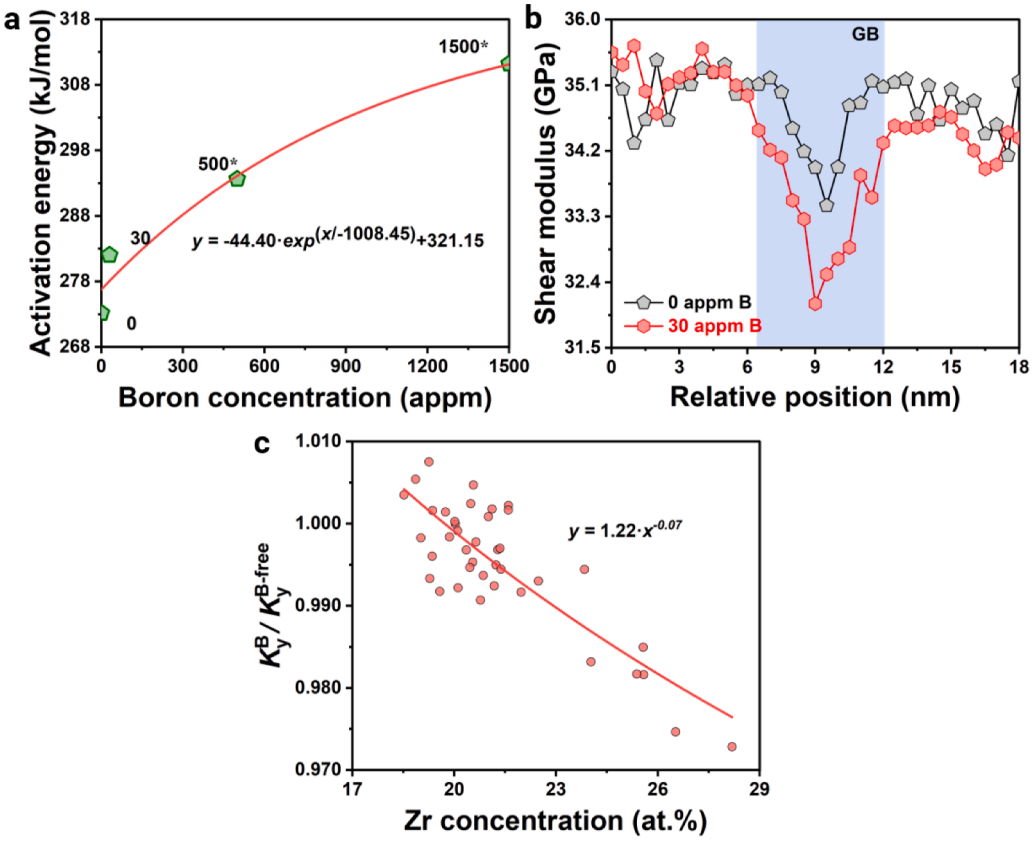

Fig. 6. (a) Calculated activation energy for grain growth as a function of B concentration. *: data used in the calculation is shown in Fig. S11. (b) Calculated shear modulus across the GB with the composition obtained from APT analysis. (c) Hall-Petch constant of non-B sample over Hall-Petch constant of B-containing sample ($K_y^B/K_y^{B-\mathrm{free}}$) plotted against Zr concentration.

A change in G^{GB} is expected due to a stronger elemental segregation of Zr and depletion of Nb/Ta at the GB in the B-doped specimen compared with the B-free material (Fig. 3). As Zr possesses the lowest shear modulus (18 GPa), compared with Nb and Ta (38 GPa for Nb and 68 GPa for Ta), a reduction in G^{GB} is anticipated and confirmed by approaching G^{GB} based on the GB composition [69,70]. To semi-quantitatively assess how B doping influences G^{GB}, a linear rule-of-mixture was used based on local GB compositions derived from APT ($G^{GB} = \sum_1^n x_i G_i$, where x_i represents the atomic percentage of i element), as direct experimental measurement of G^{GB} is challenging. G^{GB} is then determined to be 32.1 GPa in the B-doped specimen, while the B-free specimen exhibits a higher value of 33.5 GPa (Fig. 6b). It should be noted that B is not explicitly considered in the above approximation due to (1) its low concentration relative to the principal elements, and (2) the absence of boride formation [71,72]. From Eq. (11), we reveal that $\frac{K_y^B}{K_y^{B-free}} \propto \frac{G_B^{GB}}{G_{B-free}^{GB}} \propto \frac{\sum x_B^{GB}}{\sum x_{B-free}^{GB}}$, indicating that K_y decreases with the increasing Zr concentration (Fig. 6c). This result suggests that B segregation, along with Zr co-segregation, reduces K_y, thereby lowering the resistance to dislocation emission from GBs at yielding. It is worth noting that this model serves as a simplified approximation. The actual shear modulus of GBs in an HEA depends not only on composition but also on the atomic-scale structure, including local disorder, excess free volume, and solute-induced bond-strength variations, which cannot be fully captured by a simple volumetric average [73,74]. These limitations introduce

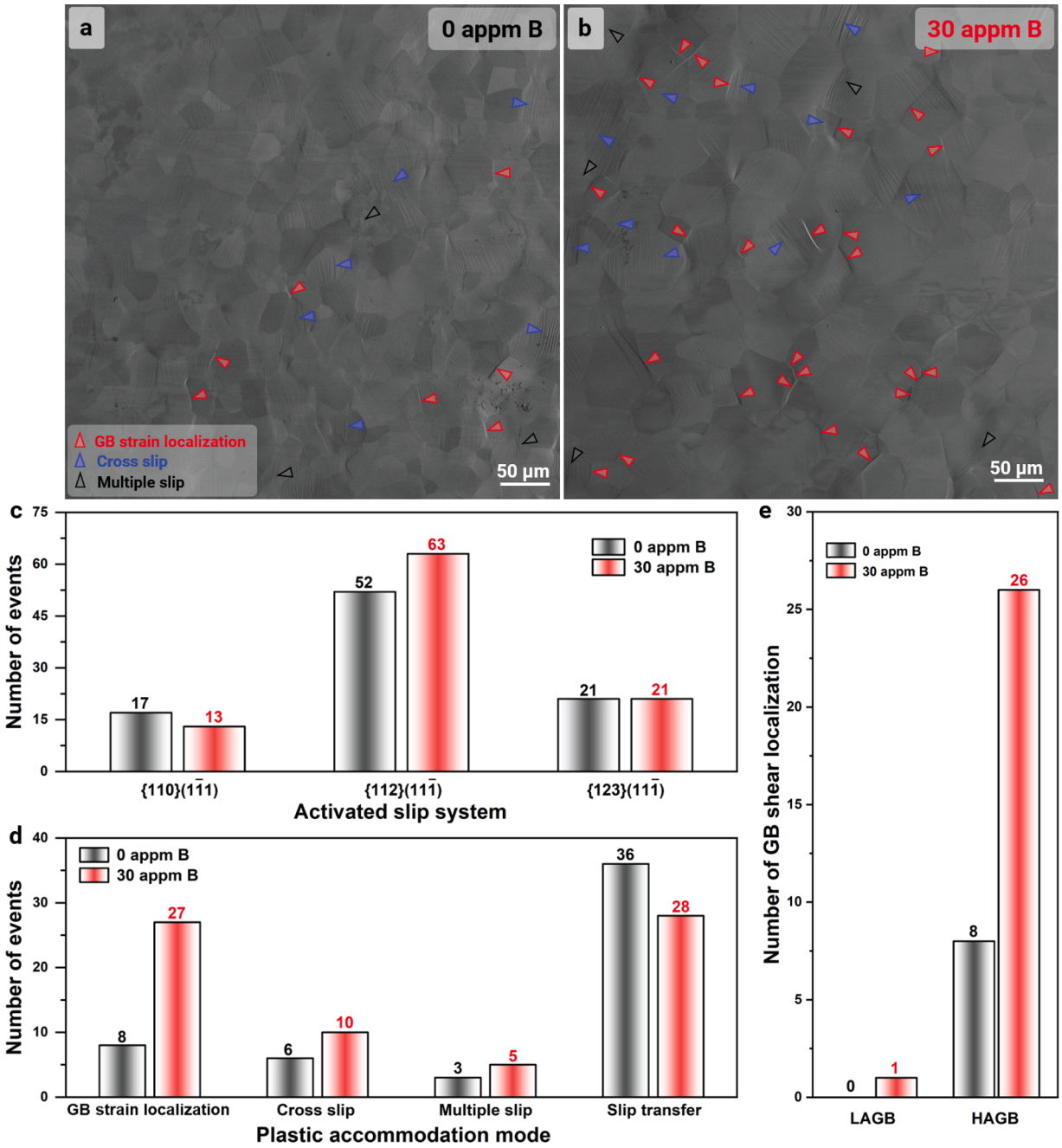

Fig. 7. Statistical analysis of plastic accommodation modes of TiNbZrHfTa HEAs with (a) 0 appm B, and (b) 30 ppm B at a strain of 2%. For improved visualization, SEM images are adjusted uniformly (+20% brightness, +20% contrast). Quantitative assessments of the (c) activated slip systems and (d) plastic accommodation modes of both the TiNbZrHfTa HEAs with 0 appm B and 30 appm B. (e) Further assessment of the GB strain localization frequency versus the types of GBs. LAGB and HAGB represent the low-angle GB and high-angle GB, respectively.

uncertainty into the absolute value of G^{GB}. However, B segregation is known to decrease the stress for dislocation generation from GBs, alleviating their strengthening effects [75–77]. Additionally, co-segregated Zr can induce local amorphization, reducing the resistance for dislocation emission from GBs [78,79]. The simplified model is able to qualitatively reflect these softening effects. Therefore, the GB ledge model provides a plausible explanation for the observed yield strength softening, which is likely attributed to B/Zr segregation at GBs. Here, the distinct roles of the intentionally doped B and the co-segregant Zr are further elaborated. We propose that B acts primarily as a segregation trigger that promotes Zr co-segregation. This hypothesis is supported by our experimental observations of a ~5 at.% increase in Zr segregation, which correlates with the yield strength softening behavior. From both thermodynamic and kinetic perspectives, B has a higher propensity for GB occupancy due to its lower segregation energy (~−1.2 eV) compared with Zr (~−0.1 eV) [80,81], and its significantly higher diffusivity ($D_B \approx 10^{-13}$ *vs.* $D_{Zr} \approx 10^{-18}$ m^2/s at 500 °C) [82,83]. Once at GBs, B promotes Zr segregation due to their strongly negative mixing enthalpy (−71 kJ/mol) relative to other principal elements [50]. However, we emphasize that the present model only reflects compositional changes, as it does not account for the structural modifications (*e.g.*, free volume, bonding strength and atomic packing) induced by segregated atoms [75–79], which are challenging to probe. Furthermore, the difficulty in decoupling the individual contributions of B and Zr introduces additional uncertainty in revealing their specific roles. These findings suggest the non-negligible role of the co-segregation elements (here, B and Zr) on mechanical properties. When deploying GB segregation engineering of doping elements, the co-segregation behavior of other alloying elements is necessary to be considered. Similar effects can also be rationalized by other Hall-Petch mechanisms, *e.g.*, the dislocation pile-up model, wherein the co-segregation of B and Zr reduces the critical stress for dislocation emission from GBs, thus compromising the strengthening contribution induced by GBs [75–78,84,85].

4.2. Activation of grain boundary strain localization upon B doping

In addition to the yield behavior, the plastic deformation behavior is also evaluated and compared. In TiNbZrHfTa refractory HEAs, dislocation slip accounts for the primary deformation mechanism to accommodate percolative bulk plastic deformation at RT. Generally, dislocation-related plasticity of BCC metals is primarily governed by the motion of a/2 < 111> screw dislocations, whose core structure is non-planar, gliding on {110}, {112}, and {123} planes, or in composite mode (pencil glide) [4,8,9]. To clarify the slip behavior of the polycrystalline refractory HEA, a large region (500 × 500 μm^2, with approximately 100 grains) at a global strain of approximately 2% was probed with respect to the quantitative assessment of slip traces (Figs. 7a and b, **Tables S3** and **S4**). Most of grains exhibit slip traces following low-indexed slip planes, such as {110}, {112}, and {123}. The {112}$(11\bar{1})$ system is determined to be the favorable slip system for plastic deformation in both the B-free and B-doped specimens (Fig. 7c), suggesting that B addition has no observable effect on the types of slip systems activated for plastic accommodation. In addition, other plastic accommodation modes, including multiple slip, cross slip, GB strain localization, and slip transfer, were further analyzed and compared between the B-free and B-doped specimens. The total plastic deformation gradient ($\mathbf{E}^P$), resulting from the plasticity micro-mechanisms that can be considered as affine shear (*e.g.*, conservative dislocation motion and mechanical twinning), is given by [86,87],

$$\mathbf{E}^P = \sum_{\alpha} \gamma^i \left(\boldsymbol{s}^i \otimes \boldsymbol{m}^i\right) \tag{12}$$

where $\boldsymbol{s}^i$ and $\boldsymbol{m}^i$ denote the orthonormal unit vectors for each plastic deformation mode *i*. γ^i represents the scalar shear strain associated with the plastic deformation mode *i*. While direct measurement of individual γ^i values is challenging, we adopted a simplified approach by quantifying slip activity based on the number of observed deformation events at the microstructural level. The frequency and occurrence of these deformation events can provide a statistical assessment of the deformation behavior, following here two simplifying key assumptions: (1) only the accommodated plastic deformation within a specific deformation mode is compared between the B-free and B-doped samples, and (2) we assume that the shear per deformation trace feature is similar for the two materials, $\gamma^i_{B-free} \approx \gamma^i_B$, given that experimental observations indicate the GB chemistry (and not the B solute state) as the main difference between these two materials.

As shown in Fig. 7d, GB strain localization becomes an additional deformation mode for accommodating plasticity in the B-doped HEA as compared with the B-free HEA. GBs, serving as a barrier against dislocation motion, are usually considered as the origin of strain localization and damage initiation once dislocations approach and concentrate on them, serving as a barrier against dislocation motion and thus resulting in stress concentration [88–90]. The associated forward stress concentration can be mitigated via highly localized strain deformation along or in the vicinity of the GB planes [91–94]. Therefore, the increase in the number of GB strain localization events in the B-doped material (from 8 to 27, see Fig. 7d) suggests that GB strain localization is also accommodating plasticity. Furthermore, GB strain localization occurs more frequently at high-angle GBs, particularly those with a misorientation angle above 30° (Fig. 7e). This characteristic is primarily attributed to the larger free volume within high-angle GBs, as free volume increases with the misorientation angle between grains. As a result, there is a stronger enrichment of B and Zr at these GBs [95,96].

While these analyses indirectly suggest the critical role of GBs in accommodating plastic deformation, a further question arises regarding the specific deformation mechanisms operating at GBs and the extent of plastic strain they accommodate. To this end, 300 × 300 μm^2 micro-grid lines with a 20-μm interval were FIB-patterned to track the deformation micro-events (Figs. 8a and b). As validated by the laser scanning confocal microscopy, the grid lines exhibit an average width of approximately 1 μm and a depth of less than 0.5 μm (Figs. 8c-h). These parameters were chosen considering the average grain sizes of the studied alloys (~65 μm) and the available recipes from the literature [94]. Under tensile loading, the deformation of the micro-grid lines was used to quantify the total grid strain along the loading axis (ε_{grid}), $\varepsilon_{grid} = \Delta L/L_0$, where ΔL and L_0 represent the change in grid length and the initial grid length.

With the microgrid pattern made on the sample surface, the local strain of each small element can be quantitatively assessed by tracking the displacement of each grid intersection. As illustrated in Fig. 9a, the displacements of each intersection point along the *x* and *y* directions can be calculated as $u^i = x^i_t - x^i_0$ and $v^i = y^i_t - y^i_0$, respectively. The Green-Lagrange strain was subsequently employed to determine the individual strain components (normal strain components (ε_{xx}, ε_{yy}, and ε_{zz}), and engineering shear strains (γ_{xy}, γ_{yz}, and γ_{zx})) and the corresponding equivalent plastic strain (ε_{eq}) [97],

$$\varepsilon_{xx} = \frac{\partial u}{\partial x} + \frac{1}{2}\left[\left(\frac{\partial u}{\partial x}\right)^2 + \left(\frac{\partial v}{\partial x}\right)^2\right] \tag{13}$$

$$\varepsilon_{yy} = \frac{\partial v}{\partial y} + \frac{1}{2}\left[\left(\frac{\partial u}{\partial y}\right)^2 + \left(\frac{\partial v}{\partial y}\right)^2\right] \tag{14}$$

$$\gamma_{xy} = \frac{1}{2}\left(\frac{\partial u}{\partial y} + \frac{\partial v}{\partial x}\right) + \frac{1}{2}\left(\frac{\partial u}{\partial x}\frac{\partial u}{\partial y} + \frac{\partial v}{\partial x}\frac{\partial v}{\partial y}\right) \tag{15}$$

$$\varepsilon_{eq} = \sqrt{\frac{2}{3}\left(\varepsilon_x{}^2 + \varepsilon_y{}^2 + \varepsilon_z{}^2\right) + \frac{1}{3}\left(\gamma_{xy}{}^2 + \gamma_{yz}{}^2 + \gamma_{zx}{}^2\right)} \tag{16}$$

Here, the displacement in the *z*-direction (ε_{zz}) cannot be directly measured using this method. However, the strain in the *z*-direction can

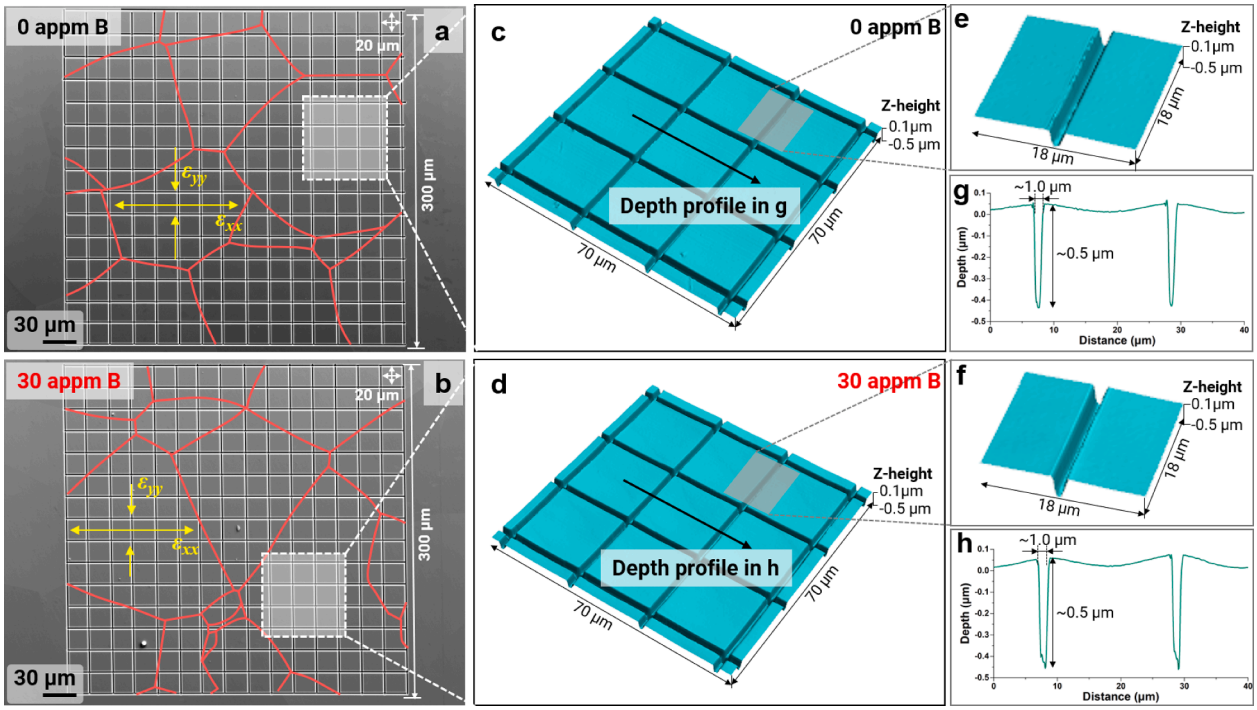

Fig. 8. Undeformed micro-gridded microstructures of TiNbZrHfTa HEAs with (a) 0 appm B and (b) 30 appm B. GBs are indicated by red solid lines, and the corresponding EBSD IPF maps of both samples are shown in Fig. S12. ε_{xx} and ε_{yy} indicate the loading direction and the transverse direction, respectively. Three-dimensional profiles acquired by laser scanning confocal microscopy validating the depth of the micro-grid lines in TiNbZrHfTa HEAs with (c, e, and g) 0 appm B and (d, f, and h) 30 appm B.

be inferred based on the assumption of constant volume during plastic deformation, expressed as $\varepsilon_{zz} = -\varepsilon_{xx} - \varepsilon_{yy}$. Considering that out-of-plane shear deformation is negligible in this study (within 4 μm, as evaluated in **Fig. S13**), ${\gamma_{yz}}^2 = {\gamma_{zx}}^2 = 0$, and ε_{eq} is therefore expressed as,

$$\varepsilon_{eq} = \sqrt{\frac{2}{3}\left({\varepsilon_{xx}}^2 + {\varepsilon_{yy}}^2 + {\varepsilon_{zz}}^2\right) + \frac{1}{3}{\gamma_{xy}}^2} \tag{17}$$

The microstructures of the micro-grids at a total grid strain of 16.5% and the corresponding ε_{eq} maps are shown in Figs. 9b-e. Before interpreting the quantitative results from the micro-grid experiments, one point needs to be clarified, since the use of surface fiducial markers for studying plastic deformation has long been criticized for its limit to unambiguously capture the bulk behavior [94,98–100]. The top surface of the sample tends to maintain a plane stress condition, allowing grains to freely undergo out-of-plane shear. Consequently, a "floating grains" phenomenon may occur, in which grains near the surface remain apparently undeformed yet can still experience substantial plastic deformation driven by the underlying material [100]. In this study, the out-of-plane displacements remain moderate for both B-free and B-doped HEAs (**Fig. S13**). In addition, the presence of noticeable slip traces in both alloys suggests that no floating grains exist within the micro-gridded region, providing cross-validation of the measured surface strains. In the B-free sample, regions of large plastic strain are primarily located within the grain interiors, whereas in the B-doped sample, significant plastic strain is mainly concentrated at the GBs. Locally, the equivalent strain in the vicinity of GBs attains values as high as 0.5 in the B-doped sample when the overall grid strain approaches approximately 16.5%. The GBs exhibiting large plastic strain distributions possess misorientation angles above 30°, consistent with the previous SEM observations (Fig. 7). The observed difference in strain distribution reveals that B addition promotes plastic strain accommodation at GBs, implying an increased contribution of GBs to overall deformation due to the alternation in GB chemistry.

The micrographs in Figs. 9f and g present the deformation details of two selected areas of interest at different grid strain levels. At a grid strain of approximately 1.1%, traits of transgranular plastic deformation are observed, as indicated by the presence of slip traces (here, only a single slip system is activated) and the slight elongation of the grid lines. As the grid strain increases to about 6.1%, multiple slip systems become active, manifested by the appearance of multiple slip traces along different directions. It is also worth noting that in the B-doped sample, distortion of the grid line also exists at the GB (with a misorientation angle of 30.4°). This distortion further intensifies as indicated by the increasingly curved grid lines when the deformation level reaches ~16.5%. Additionally, extensive slip band formation and the activation of multiple slip systems are observed in the vicinity of GBs, suggesting strong interactions between dislocations and GBs. This behavior is further indicated by the higher shear strain (γ_{xy}) distribution along the GBs compared to the normal strain component (ε_{xx}) (**Fig. S14**). In contrast, no obvious grid line mismatch is observed at the GB (with a misorientation angle of 44.9°) for the B-free sample. These detailed deformation processes indicate that the underlying mechanism is slip-assisted GB strain localization, wherein dislocations gliding from neighboring grains interact with the boundary and facilitate strain accommodation along the GB plane [38,76,101]. In addition, such behavior is more prevalent in the B-doped alloy, suggesting that the altered GB chemistry (*i.e.*, B/Zr co-segregation) may enable GBs to act as an additional pathway for accommodating plastic deformation. This tendency is primarily attributed to the decreased GB shear modulus upon B doping (Section 4.1.2), which reduces the resistance to GB shear localization during plastic flow. This GB softening thereby increases their ability to sustain higher plastic strain [76,102].

Similar trends can also be reflected from the kernel average misorientation (KAM) maps of the B-free and B-doped HEAs acquired in regions adjacent to the fracture surface (**Fig. S15**). The B-free specimen exhibits a broad KAM distribution in the interior grain, with an average KAM value of 0.757±0.023°, much higher than that (0.543±0.012°) for the B-doped one (**Fig. S15**g). In comparison, as revealed in **Fig. S15**h, a higher average KAM value (0.828±0.038°) is determined at GBs with B

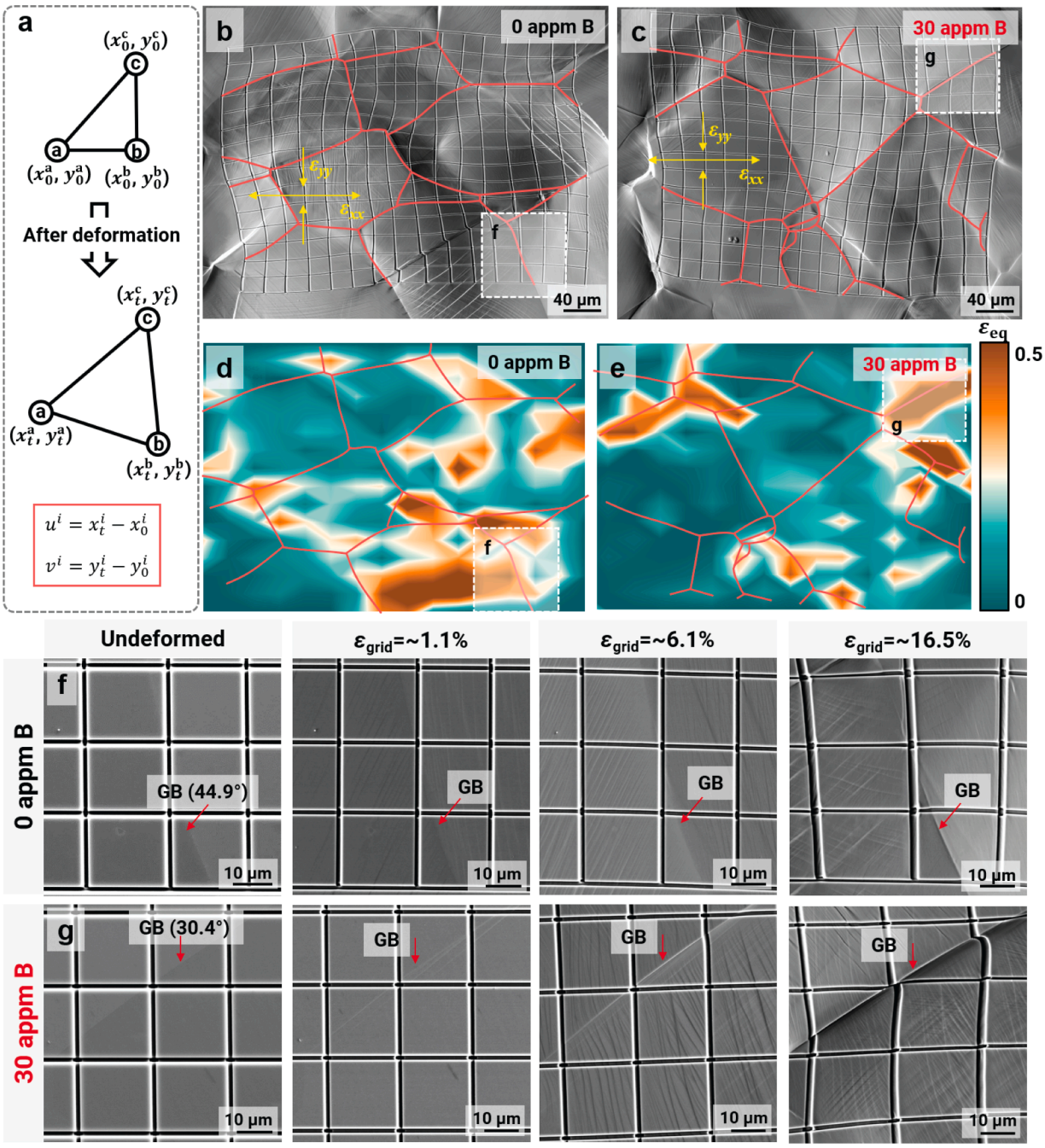

Fig. 9. (a) Deformation measurement of the grid points. SEM images of the deformed micro-grid patterns of TiNbZrHfTa HEAs with (b) 0 appm B and (c) 30 appm B, and (d-e) the corresponding equivalent plastic strain (ε_{eq}) maps with a total grid strain of ~16.5%. ε_{xx} and ε_{yy} indicate the loading direction and the transverse direction, respectively. Detailed assessments of the strain localization processes in the selected areas of TiNbZrHfTa HEAs with (f) 0 appm B and (g) 30 appm B as a function of grid strain levels. GBs are indicated by red arrows, and the corresponding misorientation angles are shown in parentheses.

addition as compared with the specimen without B addition (0.734 ±0.029°), indicating a more intense strain localization at GBs upon B doping. These strain partitioning behaviors suggest that strain tends to be redistributed between grain interiors and boundaries due to B addition. In this case, GBs can accommodate higher strain than those of the B-free case, further demonstrating that the addition of B alters the mechanisms for plastic accommodation, rendering GBs an additional mode for accommodating plastic deformation in TiNbZrHfTa.

4.3. Competition between grain boundary strain localization and slip transfer

While GB strain localization events increase with B addition, the B-doped specimen exhibits fewer slip transfer events (28 *vs.* 36 for the B-free one, see Fig. 7d), indicating a phenomenological retardation effect on slip transfers due to B segregation. These results suggest a competition between these two deformation mechanisms at GBs: slip transfer across GB *vs.* GB strain localization [91,92]. To unravel this competition, the relationship between GB strain localization and slip transfer, as well as their dependence on the presence of GB segregation, was systematically evaluated (Fig. 10). The Luster-Morris geometric compatibility

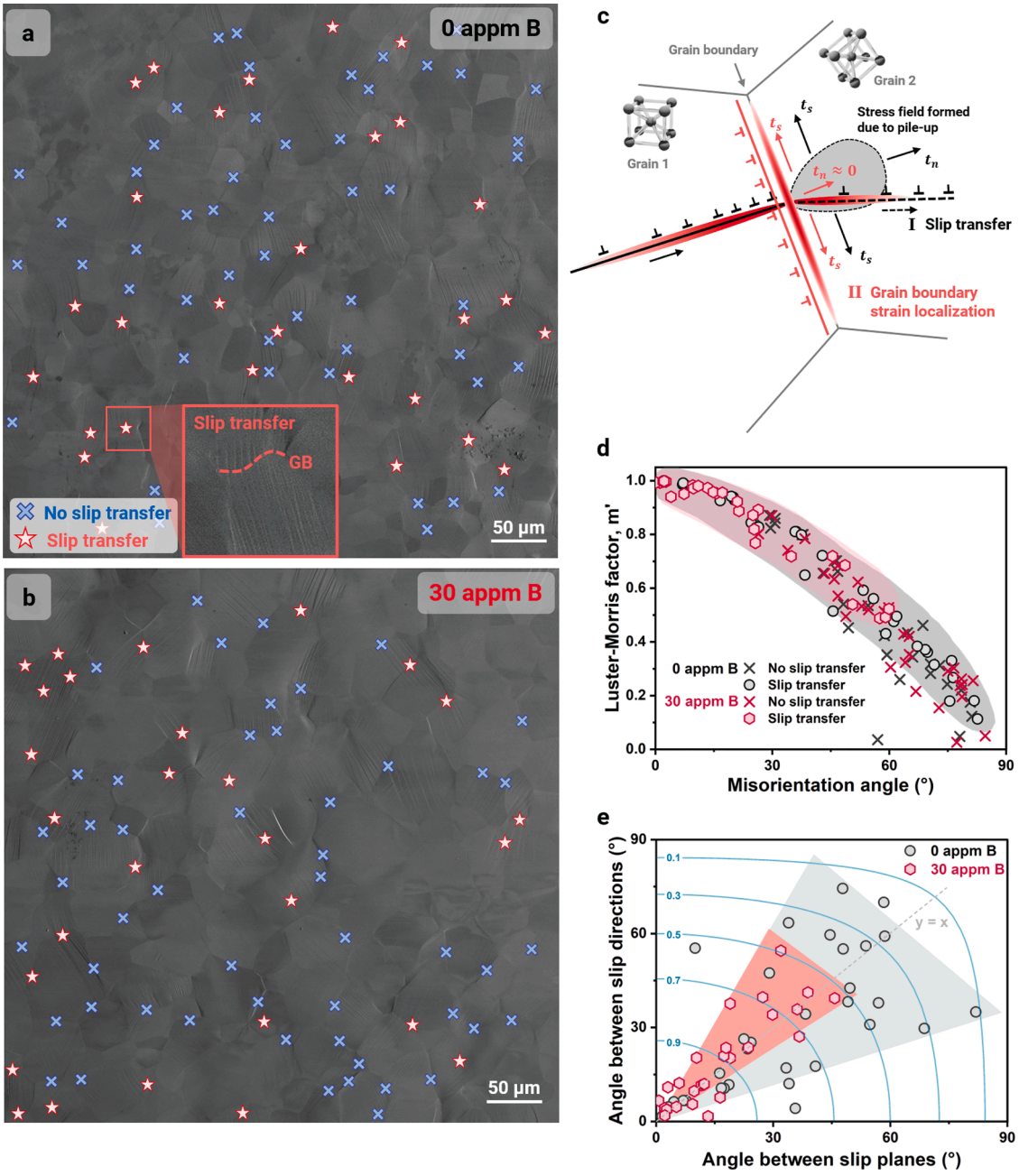

Fig. 10. Statistical analysis of slip transfer activities of TiNbZrHfTa HEAs with (a) 0 appm B, and (b) 30 appm B at a strain of 2%. Insert in (a) shows an enlarged view of one slip transfer case. For improved visualization, SEM images are adjusted uniformly (+20% brightness, +20% contrast). (c) Schematic diagram demonstrating the competition between slip transfer and GB strain localization. (d) Luster-Morris factor (m') versus misorientation angle for all surveyed grain couples. (e) Geometric correlation chart concerning the angles between slip directions and slip planes for all the surveyed grain couples with slip transfer.

factor (m') was employed to quantify the condition for slip transfer micro-events [103],

$$m' = \left[\left(g_1^{-1}\cdot \mathbf{s}_1\right)\cdot\left(g_2^{-1}\cdot \mathbf{s}_2\right)\right]\cdot\left[\left(g_1^{-1}\cdot \mathbf{n}_1\right)\cdot\left(g_2^{-1}\cdot \mathbf{n}_2\right)\right] \tag{18}$$

which considers the misalignment between slip directions at the individual grain ($\mathbf{s}_1$ and $\mathbf{s}_2$) together with the misalignment of these corresponding slip plane normals ($\mathbf{n}_1$ and $\mathbf{n}_2$). When m' closes to 1, it indicates a high tendency for slip transfer across GBs. Otherwise, the slip transfer is suppressed for an m' value close to 0. Furthermore, the misalignment angle between the slip directions (κ) and the misalignment angle between the slip normals (ψ) can also be determined through:

$$\kappa = \arccos\left[\left(g_1^{-1}\cdot \mathbf{s}_1\right)\cdot\left(g_2^{-1}\cdot \mathbf{s}_2\right)\right] \tag{19}$$

$$\psi = \arccos\left[\left(g_1^{-1}\cdot \mathbf{n}_1\right)\cdot\left(g_2^{-1}\cdot \mathbf{n}_2\right)\right] \tag{20}$$

To ensure statistical robustness, at least 20 grains exhibiting slip transfer events were analyzed and the corresponding crystallographic details were summarized in **Tables S5-S7**. An inverse correlation of m' with the misorientation angle is observed, suggesting a geometrical dependency for slip transfer (Fig. 10d), *i.e.*, slip transfer is favored for low-angle GBs (LAGBs, $< 15°$). This dependency is consistent with the literature reported on single-phase BCC metals and also FCC pure metals like Al and Ni [38,91,104,105]. This behavior is primarily ascribed to the partial coherency of the elastic strain fields that characterize the LAGBs [87,106]. This feature restricts dislocation motion within LAGBs. As a result, LAGBs act as semipermeable barriers to dislocation

transmission, while simultaneously accommodating crystallographic misorientation through structured dislocation arrays. A closer inspection of Fig. 10d indicates that the role of B in altering the slip transfer response: datum points tend to distribute at misorientation angles below 60° (*i.e.*, high m') in the B-doped HEA as compared with the B-free one (from 0 to 90°). This tendency suggests a more restrictive local geometric confinement of slip transfer due to B addition. Such a change in deformation behavior can be rationalized by the facts that: (1) the alternation of GB chemistry (*i.e.*, B/Zr segregation) may influence configurations of GBs (*e.g.*, GB phases, GB structures), potentially increasing the critical stress required for slip transfer across GBs [21,107]; (2) B/Zr atoms preferentially decorate dislocation cores, reducing dislocation mobility and slip transfer efficiency [21]. However, further systematic investigations are necessary to fully unravel the underlying mechanisms, which are beyond the scope of this study.

Fig. 10d further shows that GB-aided forward stress alleviation via slip transfer is hindered upon B addition, necessitating an alternative deformation pathway at GBs. This feature implies the increased strain localization at GBs upon B addition. Therefore, in the B-doped HEA, GB strain localization is prone to occur primarily at GBs where adjacent grains exhibit slip traces that are either parallel to or highly intersecting with the GBs. This phenomenon acts as an additional mechanism for accommodating plastic deformation, with local KAM values of grain-to-grain mismatch reaching up to 2.082±0.178° (see **Fig. S15**h). For a more precise quantification, we also computed the ψ versus κ diagram, assessing the respective contributions from slip direction misalignment and slip plane misalignment. A greater tolerance to geometrical alignments, including both the slip direction ($0° < \kappa < 76°$) and slip plane ($0° < \psi < 83°$) misalignments, can be revealed for the B-free specimen as compared with the B-doped one (lower than 56° and 48° for κ and ψ, respectively). Upon B doping, the sensitivity of the slip transfer to ψ is lower than κ. This difference may be due to the B/Zr segregation at GBs (*e.g.*, the change in GB structure, or the interaction between segregated atoms and dislocations), as ψ quantifies the possibility of local GB plane distortion to accommodate the imposed deformation states [21]. Additionally, the frequency of slip transfer occurring within the contour line with an isovalue of 0.9 (shown in blue lines) of the B-doped HEA is 53.8%, significantly higher than that of the B-free HEA (29.0%). This behavior further confirms a stronger geometrical dependence for slip transfer in the B-doped case. Such a correlation indicates that upon B doping, the B and Zr co-segregation tends to facilitate the plastic deformation at or near GBs instead of the slip transfer across GBs. A plausible mechanism can be that the stored dislocations in the vicinity of GBs are mainly absorbed and driven to glide along GBs, where GB segregation promotes this process [21,105]. In this scenario, the dislocation behavior at GBs is influenced by GB segregation as the GB chemistry and the energy landscape at these interfaces are altered [21].

5. Conclusion

In this study, the mechanical behavior in a polycrystalline TiNbZrHfTa refractory high-entropy alloy (HEA) with the addition of 30 appm boron (B) was systematically and quantitatively investigated and compared with the B-free reference sample. The major findings are summarized as follows:

(1) The ppm-level addition of B (here, 30 appm) could result in a reduction in grain size from 69.9 ± 27.2 μm to 53.9 ± 23.5 μm due to the solute drag effect of B on grain growth. The grain boundary (GB) chemistry was significantly altered upon B doping, where the co-segregation of B (1.98 at.%) and Zr (up to 28.20 at.%) accompanied by the depletion of Ta (by 3.36 at.%) and Nb (by 3.27 at.%) was revealed with the aid of atom probe tomography. The lower mixing enthalpy between B and Zr primarily contributed to the co-segregation behavior.

(2) Yield strength softening was observed upon B addition with a reduction in yield strength by ~6.2 ± 0.7%. This softening is mainly due to a reduction in the Hall-Petch coefficient caused by a change in GB chemistry (B/Zr co-segregation). The co-segregation reduces the shear modulus at the GB, facilitating dislocation emission. Such a reduction in yield strength surpasses the strengthening effect induced by grain refinement.

(3) GBs actively accommodate plastic deformation in the B-doped refractory HEA, exhibiting as slip-mediated GB strain localization, which was identified via the quantitative assessment of the plastic deformation modes. This change in plastic accommodation mechanisms as compared with the B-free specimen suggested the predominant role of the local chemistry at GBs in the plastic deformation mechanisms in the HEA. Additionally, the slip direction misalignment (κ) and slip normal misalignment (ψ) relationships of the surveyed slip traces revealed a more stringent local geometric confinement of slip transfer upon B doping as compared with the B-free case. Such a constraint suggested a competition between slip transfer and GB strain localization, further confirming the unambiguous role of elemental segregation in altering the slip transfer response.

These findings highlight the impact of ppm-level B doping on the macroscopic mechanical performance of the polycrystalline TiNbZrHfTa refractory HEAs. The observed changes in microscopic deformation modes illuminate the interplay between GB chemistry and plasticity mechanisms, offering insights into the design of advanced materials. Thus, this work sheds light on the GB segregation engineering strategies aimed at optimizing the mechanical performance of complex alloys.

CRediT authorship contribution statement

Chengguang Wu: Writing – review & editing, Writing – original draft, Visualization, Methodology, Investigation, Formal analysis, Data curation. **Shaolou Wei:** Writing – review & editing, Supervision, Formal analysis, Conceptualization. **Loïc Perrière:** Writing – review & editing, Resources, Investigation. **Jean-Philippe Couzinié:** Writing – review & editing, Resources, Investigation. **Dirk Ponge:** Writing – review & editing, Supervision. **Yan Ma:** Writing – review & editing, Supervision, Project administration, Conceptualization. **Dierk Raabe:** Writing – review & editing, Supervision, Project administration, Funding acquisition.

Declaration of competing interest

The authors declare that they have no known competing financial interests or personal relationships that could have appeared to influence the work reported in this paper.

Acknowledgements

Synchrotron X-ray diffraction measurements were carried out at beamline P02.1, PETRA III of Deutsches Elektronen-Synchrotron (DESY, proposal Nos. I-20230183 and I-20231121). The kind help on sample preparation and subsequent SEM-related characterization from Katja Angenendt and Christian Broβ at the Max Planck Institute for Sustainable Materials is gratefully acknowledged. C.G.W. would also thank Unai Aizpurua for his help on data curation at the beginning of this work. C.G.W. would like to acknowledge the financial support from the Chinese Scholarship Council (No. 202106780003). Y.M. and D.R. would like to acknowledge the financial funding of Deutsche Forschungsgemeinschaft (DFG) within the Priority Programme 2006 (Compositionally Complex Alloys—High Entropy Alloys, SPP2006-HEA-CCA). S.L.W. thanks the Alexander von Humboldt Research Fellowship (hosted by D.R.) for the financial support. The lively discussion and technical exchange with Dr. Guillaume Hachet, Dr. Jing Rao, and Dr. Yi

Hu from Max Planck Institute for Sustainable Materials are also greatly appreciated.

Supplementary materials

Supplementary material associated with this article can be found, in the online version, at doi:10.1016/j.actamat.2026.122210.

References

[1] S.Eswarappa Prameela, T.M. Pollock, D. Raabe, M.A. Meyers, A. Aitkaliyeva, K. L. Chintersingh, Z.C. Cordero, L. Graham-Brady, Materials for extreme environments, Nat. Rev. Mater. 8 (2) (2023) 81–88.
[2] E.P. George, D. Raabe, R.O. Ritchie, High-entropy alloys, Nat. Rev. Mater. 4 (8) (2019) 515–534.
[3] S. Wei, S.J. Kim, J. Kang, Y. Zhang, Y. Zhang, T. Furuhara, E.S. Park, C.C. Tasan, Natural-mixing guided design of refractory high-entropy alloys with as-cast tensile ductility, Nat. Mater. 19 (11) (2020) 1175–1181.
[4] A. Argon, Strengthening Mechanisms in Crystal Plasticity, OUP Oxford, 2007.
[5] O. Senkov, G. Wilks, D. Miracle, C. Chuang, P. Liaw, Refractory high-entropy alloys, Intermetallics (Barking) 18 (9) (2010) 1758–1765.
[6] O.N. Senkov, D.B. Miracle, K.J. Chaput, J.P. Couzinie, Development and exploration of refractory high entropy alloys—A review, J. Mater. Res. 33 (19) (2018) 3092–3128.
[7] O. Senkov, S. Semiatin, Microstructure and properties of a refractory high-entropy alloy after cold working, J. Alloys Compd. 649 (2015) 1110–1123.
[8] G. Gottstein, Physical Foundations of Materials Science, Springer, 2004.
[9] D. Hull, D.J. Bacon, Introduction to Dislocations, Elsevier, 2011.
[10] Y. Zou, S. Maiti, W. Steurer, R. Spolenak, Size-dependent plasticity in an Nb25Mo25Ta25W25 refractory high-entropy alloy, Acta Mater. 65 (2014) 85–97.
[11] O.N. Senkov, C. Woodward, D.B. Miracle, Microstructure and properties of aluminum-containing refractory high-entropy alloys, JOM 66 (10) (2014) 2030–2042.
[12] C. Lee, Y. Chou, G. Kim, M.C. Gao, K. An, J. Brechtl, C. Zhang, W. Chen, J. D. Poplawsky, G. Song, Y. Ren, Y.C. Chou, P.K. Liaw, Lattice-distortion-enhanced yield strength in a refractory high-entropy alloy, Adv. Mater. 32 (49) (2020) 2004029.
[13] Z.D. Han, N. Chen, S.F. Zhao, L.W. Fan, G.N. Yang, Y. Shao, K.F. Yao, Effect of Ti additions on mechanical properties of NbMoTaW and VNbMoTaW refractory high entropy alloys, Intermetallics (Barking) 84 (2017) 153–157.
[14] W. Guo, B. Liu, Y. Liu, T. Li, A. Fu, Q. Fang, Y. Nie, Microstructures and mechanical properties of ductile NbTaTiV refractory high entropy alloy prepared by powder metallurgy, J. Alloys Compd. 776 (2019) 428–436.
[15] C. Zhang, H. Wang, X. Wang, Y.T. Tang, Q. Yu, C. Zhu, M. Xu, S. Zhao, R. Kou, X. Wang, B.E. MacDonald, R.C. Reed, K.S. Vecchio, P. Cao, T.J. Rupert, E. J. Lavernia, Strong and ductile refractory high-entropy alloys with super formability, Acta Mater. 245 (2023) 118602.
[16] H. Huang, Y. Wu, J. He, H. Wang, X. Liu, K. An, W. Wu, Z. Lu, Phase-transformation ductilization of brittle high-entropy alloys via metastability engineering, Adv. Mater. 29 (30) (2017) 1701678.
[17] C.C. Juan, M.H. Tsai, C.W. Tsai, W.L. Hsu, C.M. Lin, S.K. Chen, S.J. Lin, J.W. Yeh, Simultaneously increasing the strength and ductility of a refractory high-entropy alloy via grain refining, Mater. Lett. 184 (2016) 200–203.
[18] D. Raabe, Z. Li, D. Ponge, Metastability alloy design, MRS Bulletin 44 (4) (2019) 266–272.
[19] S. Wei, F. He, C.C. Tasan, Metastability in high-entropy alloys: a review, J. Mater. Res. 33 (19) (2018) 2924–2937.
[20] M. Seah, E. Hondros, Grain boundary segregation, in: Proceedings of the Royal Society of London. A. Mathematical and Physical Sciences 335, 1973, pp. 191–212.
[21] D. Raabe, M. Herbig, S. Sandlöbes, Y. Li, D. Tytko, M. Kuzmina, D. Ponge, P. P. Choi, Grain boundary segregation engineering in metallic alloys: a pathway to the design of interfaces, Curr. Opin. Solid State Mater. Sci. 18 (4) (2014) 253–261.
[22] M. Seah, Interface adsorption, embrittlement and fracture in metallurgy: a review, Surf. Sci. 53 (1) (1975) 168–212.
[23] M. Seah, Adsorption-induced interface decohesion, Acta Metallurgica 28 (7) (1980) 955–962.
[24] P. Lejček, S. Hofmann, Thermodynamics and structural aspects of grain boundary segregation, Crit. Rev. Solid State Mater. Sci. 20 (1) (1995) 1–85.
[25] M. Seah, Segregation and the strength of grain boundaries, in: Proceedings of the Royal Society of London. A. Mathematical and Physical Sciences 349, 1976, pp. 535–554.
[26] Y. Tan, R. Chen, H. Fang, Y. Liu, H. Cui, Y. Su, J. Guo, H. Fu, Enhanced strength and ductility in Ti46Al4Nb1Mo alloys via boron addition, J. Mater. Sci. Technol. 102 (2022) 16–23.
[27] J. Pang, H. Zhang, L. Zhang, Z. Zhu, H. Fu, H. Li, A. Wang, Z. Li, H. Zhang, Simultaneous enhancement of strength and ductility of body-centered cubic TiZrNb multi-principal element alloys via boron-doping, J. Mater. Sci. Technol. 78 (2021) 74–80.
[28] Z. Wang, H. Wu, Y. Wu, H. Huang, X. Zhu, Y. Zhang, H. Zhu, X. Yuan, Q. Chen, S. Wang, Solving oxygen embrittlement of refractory high-entropy alloy via grain boundary engineering, Materials Today 54 (2022) 83–89.
[29] J.B. Seol, J.W. Bae, Z. Li, J.C. Han, J.G. Kim, D. Raabe, H.S. Kim, Boron doped ultrastrong and ductile high-entropy alloys, Acta Mater. 151 (2018) 366–376.
[30] Y. Qi, T. Cao, H. Zong, Y. Wu, L. He, X. Ding, F. Jiang, S. Jin, G. Sha, J. Sun, Enhancement of strength-ductility balance of heavy Ti and Al alloyed FeCoNiCr high-entropy alloys via boron doping, J. Mater. Sci. Technol. 75 (2021) 154–163.
[31] L. Ma, X. Zhang, B. Pu, D. Zhao, C. He, N. Zhao, Achieving the strength-ductility balance of boron nitride nanosheets/Al composite by designing the synergistic transition interface and intragranular reinforcement distribution, Compos. Part B Eng. 246 (2022) 110243.
[32] S. Wei, K.S. Kim, J. Foltz, C.C. Tasan, Discovering pyramidal treasures: multi-scale design of high strength-ductility titanium alloys, Adv. Mater. (2024) 2406382.
[33] G. Zhu, L. Wang, H. Zhou, J. Wang, Y. Shen, P. Tu, H. Zhu, W. Liu, P. Jin, X. Zeng, Improving ductility of a Mg alloy via non-basal< a>slip induced by Ca addition, Int. J. Plast. 120 (2019) 164–179.
[34] P.M. Anderson, J.P. Hirth, J. Lothe, Theory of Dislocations, Cambridge University Press, 2017.
[35] Q. He, S. Yoshida, S. Okajo, M. Tanaka, N. Tsuji, Characteristic dislocation slip behavior in polycrystalline HfNbTiZr refractory medium entropy alloy, J. Mater. Sci. Technol. 210 (2025) 29–39.
[36] L. Wang, Y. Yang, P. Eisenlohr, T. Bieler, M. Crimp, D. Mason, Twin nucleation by slip transfer across grain boundaries in commercial purity titanium, Metal. Mater. Trans. A 41 (2) (2010) 421–430.
[37] S. Wei, G. Zhu, C.C. Tasan, Slip-twinning interdependent activation across phase boundaries: an in-situ investigation of a Ti-Al-V-Fe (α+ β) alloy, Acta Mater. 206 (2021) 116520.
[38] S. Wei, J. Kim, C.C. Tasan, In-situ investigation of plasticity in a Ti-Al-V-Fe (α+ β) alloy: slip mechanisms, strain localization, and partitioning, Int. J. Plast. 148 (2022) 103131.
[39] C. Marichal, H. Van Swygenhoven, S. Van Petegem, C. Borca, {110} Slip with {112} slip traces in bcc Tungsten, Sci. Rep. 3 (1) (2013) 2547.
[40] H.J. Bunge, Texture Analysis in Materials science: Mathematical Methods, Elsevier, 2013.
[41] S. Wei, J. Kim, C.C. Tasan, Boundary micro-cracking in metastable Fe45Mn35Co10Cr10 high-entropy alloys, Acta Mater. 168 (2019) 76–86.
[42] A.C. Dippel, H.P. Liermann, J.T. Delitz, P. Walter, H. Schulte-Schrepping, O. H. Seeck, H. Franz, Beamline P02. 1 at PETRA III for high-resolution and high-energy powder diffraction, J. Synchrotron. Radiat. 22 (3) (2015) 675–687.
[43] B.H. Toby, R.B. Von Dreele, GSAS-II: the genesis of a modern open-source all purpose crystallography software package, J. Appl. Crystallogr. 46 (2) (2013) 544–549.
[44] G. Williamson, W. Hall, X-ray line broadening from filed aluminium and wolfram, Acta Metallurgica 1 (1) (1953) 22–31.
[45] J.I. Langford, A. Wilson, Scherrer after sixty years: a survey and some new results in the determination of crystallite size, Appl. Crystal. 11 (2) (1978) 102–113.
[46] G. Williamson, R. Smallman III, Dislocation densities in some annealed and cold-worked metals from measurements on the X-ray Debye-Scherrer spectrum, Philos. Mag. 1 (1) (1956) 34–46.
[47] M.H. Tsai, J.W. Yeh, High-entropy alloys: a critical review, Mater. Res. Lett. 2 (3) (2014) 107–123.
[48] P. Thirathipviwat, G. Song, J. Bednarcik, U. Kühn, T. Gemming, K. Nielsch, J. Han, Compositional complexity dependence of dislocation density and mechanical properties in high entropy alloy systems, Prog. Nat. Sci. Mater. Int. 30 (4) (2020) 545–551.
[49] G. Dirras, J. Gubicza, A. Heczel, L. Lilensten, J.P. Couzinié, L. Perrière, I. Guillot, A. Hocini, Microstructural investigation of plastically deformed Ti20Zr20Hf20Nb20Ta20 high entropy alloy by X-ray diffraction and transmission electron microscopy, Mater. Charact. 108 (2015) 1–7.
[50] A. Takeuchi, A. Inoue, Classification of bulk metallic glasses by atomic size difference, heat of mixing and period of constituent elements and its application to characterization of the main alloying element, Mater. Trans. 46 (12) (2005) 2817–2829.
[51] G. Saada, Cross-slip and work hardening of fcc crystals, Mater. Sci. Eng. A 137 (1991) 177–183.
[52] W. Püschl, Models for dislocation cross-slip in close-packed crystal structures: a critical review, Prog. Mater. Sci. 47 (4) (2002) 415–461.
[53] E.P. George, W.A. Curtin, C.C. Tasan, High entropy alloys: a focused review of mechanical properties and deformation mechanisms, Acta Mater. 188 (2020) 435–474.
[54] E. Hall, The deformation and ageing of mild steel: III discussion of results, Proc. Phys. Soc. Sect. B 64 (9) (1951) 747.
[55] N.J. Petch, The cleavage strength of polycrystals, J. Iron Steel Inst. 174 (1953) 25–28.
[56] N. Hansen, Hall–Petch relation and boundary strengthening, Scr. Mater. 51 (8) (2004) 801–806.
[57] F.J. Humphreys, M. Hatherly, Recrystallization and Related Annealing Phenomena, elsevier, 2012.
[58] R. Kirchheim, Reducing grain boundary, dislocation line and vacancy formation energies by solute segregation: II. Experimental evidence and consequences, Acta Mater. 55 (15) (2007) 5139–5148.
[59] F. Liu, R. Kirchheim, Nano-scale grain growth inhibited by reducing grain boundary energy through solute segregation, J. Cryst. Growth 264 (1–3) (2004) 385–391.
[60] J. Burke, D. Turnbull, Recrystallization and grain growth, Prog. Metal Phys. 3 (1952) 220–292.

[61] H. Atkinson, Overview no. 65: theories of normal grain growth in pure single phase systems, Acta Metallurgica 36 (3) (1988) 469–491.
[62] H. Adrian, F. Pickering, Effect of titanium additions on austenite grain growth kinetics of medium carbon V–Nb steels containing 0· 008–0· 018% N, Mater. Sci. Tech. 7 (2) (1991) 176–182.
[63] M. Hillert, On the theory of normal and abnormal grain growth, Acta Metallurgica 13 (3) (1965) 227–238.
[64] L. Murr, Dislocation ledge sources: dispelling the myth of Frank–Read source importance, Metal. Mater. Trans. A 47 (2016) 5811–5826.
[65] J.C. Li, High-angle tilt boundary—A dislocation core model, J. Appl. Phys. 32 (3) (1961) 525–541.
[66] V. Borovikov, M.I. Mendelev, A.H. King, Effects of grain boundary disorder on dislocation emission, Mater. Lett. 237 (2019) 303–305.
[67] A. Lasalmonie, J. Strudel, Influence of grain size on the mechanical behaviour of some high strength materials, J. Mater. Sci. 21 (6) (1986) 1837–1852.
[68] X. Zhou, S. Kumar, S. Zhang, X. Chen, B. Gault, G. Dehm, T. Hickel, D. Raabe, Boron triggers grain boundary structural transformation in steel, Nat. Commun. 16 (1) (2025) 6927.
[69] Y. Hao, S. Li, B. Sun, M. Sui, R. Yang, Ductile titanium alloy with low Poisson's ratio, Phys. Rev. Lett. 98 (21) (2007) 216405.
[70] B.T. Wang, P. Zhang, H.Y. Liu, W.D. Li, P. Zhang, First-principles calculations of phase transition, low elastic modulus, and superconductivity for zirconium, arXiv preprint arXiv:1007.4913 (2010).
[71] B. Kang, T. Kong, N.H. Dan, D.D. Phuong, H.J. Ryu, S.H. Hong, Effect of boron addition on the microstructure and mechanical properties of refractory Al0.1CrNbVMo high-entropy alloy, Int. J. Refract. Metal Hard Mater. 100 (2021) 105636.
[72] X.F. Zhou, Y. Tian, H.T. Wang, Large shear strength enhancement of gamma-boron by normal compression, J. Superhard Mater. 33 (2011) 401–408.
[73] S.M. Das, P. Harrison, S. Kiranbabu, X. Zhou, W. Ludwig, E.F. Rauch, M. Herbig, C.H. Liebscher, Correlating grain boundary character and composition in 3-dimensions using 4D-scanning precession electron diffraction and atom probe tomography, Small. Methods 9 (5) (2025) 2401650.
[74] D. Brandon, The structure of high-angle grain boundaries, Acta Metallurgica 14 (11) (1966) 1479–1484.
[75] T. Lee, I. Robertson, H. Birnbaum, Interaction of dislocations with grain boundaries in Ni3Al, Acta Metallurgica et Materialia 40 (10) (1992) 2569–2579.
[76] E. Schulson, T. Weihs, I. Baker, H. Frost, J. Horton, Grain boundary accommodation of slip in Ni3Al containing boron, Acta Metallurgica 34 (7) (1986) 1395–1399.
[77] C. Lee, G. Han, R. Smallman, D. Feng, J. Lai, The influence of boron-doping on the effectiveness of grain boundary hardening in Ni3Al, Acta Mater. 47 (6) (1999) 1823–1830.
[78] V. Borovikov, M.I. Mendelev, A.H. King, Effects of Ag and Zr solutes on dislocation emission from Σ11 (332)[110]symmetric tilt grain boundaries in Cu: bigger is not always better, Int. J. Plast. 109 (2018) 79–87.
[79] L. Qian, J. Zhang, W. Yang, Y. Wang, K. Chan, X.S. Yang, Maintaining grain boundary segregation-induced strengthening effect in extremely fine nanograined metals, Nano Lett. 25 (13) (2025) 5493–5501.
[80] Y. Shi, D.A. Alshammari, C. Lei, H.K. Thabet, H. Xue, F. Tang, First-principles investigation on solute co-segregations and their strengthening grain boundary roles in stable nanocrystalline copper, Adv. Compos. Hybrid. Mater. 7 (5) (2024) 137.
[81] Z. Huang, F. Chen, Q. Shen, L. Zhang, T.J. Rupert, Uncovering the influence of common nonmetallic impurities on the stability and strength of a Σ5 (310) grain boundary in Cu, Acta Mater. 148 (2018) 110–122.
[82] M.I. Razumovsky, B.S. Bokstein, A.O. Rodin, A.V. Khvan, Interdiffusion in refractory metal system with a BCC lattice: Ti/TiZrHfNbTaMo, Entropy 25 (3) (2023) 490.
[83] Y. Duan, Y. Wu, M. Peng, H. Qi, The interstitial diffusion behaviors and mechanisms of boron in α-Ti and β-Ti: a first-principles calculation, Comput. Mater. Sci. 184 (2020) 109866.
[84] R. Armstrong, I. Codd, R. Douthwaite, N. Petch, The plastic deformation of polycrystalline aggregates, Philos. Mag. J. Theo. Exp. Appl. Phys. 7 (73) (1962) 45–58.
[85] D. Wu, J. Zhang, J. Huang, H. Bei, T.G. Nieh, Grain-boundary strengthening in nanocrystalline chromium and the Hall–Petch coefficient of body-centered cubic metals, Scr. Mater. 68 (2) (2013) 118–121.
[86] M.E. Gurtin, E. Fried, L. Anand, The Mechanics and Thermodynamics of Continua, Cambridge university press, 2010.
[87] F. Roters, P. Eisenlohr, L. Hantcherli, D.D. Tjahjanto, T.R. Bieler, D. Raabe, Overview of constitutive laws, kinematics, homogenization and multiscale methods in crystal plasticity finite-element modeling: theory, experiments, applications, Acta Mater. 58 (4) (2010) 1152–1211.
[88] T.Y. Thomas, Plastic Flow and Fracture in Solids by Tracy Y Thomas, Elsevier, 1961.
[89] S.D. Antolovich, R.W. Armstrong, Plastic strain localization in metals: origins and consequences, Prog. Mater. Sci. 59 (2014) 1–160.
[90] C.C. Tasan, J.P. Hoefnagels, M. Diehl, D. Yan, F. Roters, D. Raabe, Strain localization and damage in dual phase steels investigated by coupled in-situ deformation experiments and crystal plasticity simulations, Int. J. Plast. 63 (2014) 198–210.
[91] M. Linne, A. Venkataraman, M. Sangid, S. Daly, Grain boundary sliding and slip transmission in high purity aluminum, Exp. Mech. 59 (2019) 643–658.
[92] M.A. Linne, T.R. Bieler, S. Daly, The effect of microstructure on the relationship between grain boundary sliding and slip transmission in high purity aluminum, Int. J. Plast. 135 (2020) 102818.
[93] R. Gates, The role of grain boundary dislocations in grain boundary sliding, Acta Metallurgica 21 (7) (1973) 855–864.
[94] S. Wei, C.C. Tasan, On the plastic deformation of a CoCrFeNiW-C alloy at elevated temperatures: part II. Grain boundary sliding and damage mechanisms, Acta Mater. 252 (2023) 118898.
[95] T. Watanabe, T. Murakami, S. Karashima, Misorientation dependence of grain boundary segregation, Scripta Metallurgica 12 (4) (1978) 361–365.
[96] T. Duh, J. Kai, F. Chen, L. Wang, Effects of grain boundary misorientation on the solute segregation in austenitic stainless steels, J. Nucl. Mater. 258 (1998) 2064–2068.
[97] N. Ishikawa, K. Yasuda, H. Sueyoshi, S. Endo, H. Ikeda, T. Morikawa, K. Higashida, Microscopic deformation and strain hardening analysis of ferrite–bainite dual-phase steels using micro-grid method, Acta Mater. 97 (2015) 257–268.
[98] M. Charpagne, J. Hestroffer, A. Polonsky, M. Echlin, D. Texier, V. Valle, I. Beyerlein, T. Pollock, J. Stinville, Slip localization in Inconel 718: a three-dimensional and statistical perspective, Acta Mater. 215 (2021) 117037.
[99] Z. Zhao, M. Ramesh, D. Raabe, A. Cuitino, R. Radovitzky, Investigation of three-dimensional aspects of grain-scale plastic surface deformation of an aluminum oligocrystal, Int. J. Plast. 24 (12) (2008) 2278–2297.
[100] M. Mayo, W. Nix, Direct observation of superplastic flow mechanisms in torsion, Acta Metallurgica 37 (4) (1989) 1121–1134.
[101] Z. Shen, R. Wagoner, W. Clark, Dislocation and grain boundary interactions in metals, Acta Metallurgica 36 (12) (1988) 3231–3242.
[102] C.T. Liu, C. White, J. Horton, Effect of boron on grain-boundaries in Ni3Al, Acta Metallurgica 33 (2) (1985) 213–229.
[103] J. Luster, M. Morris, Compatibility of deformation in two-phase Ti-Al alloys: dependence on microstructure and orientation relationships, Metal. Mater. Trans. A 26 (1995) 1745–1756.
[104] Y. Li, P. Gao, J. Yu, S. Jin, S. Chen, M. Zhan, Mesoscale deformation mechanisms in relation with slip and grain boundary sliding in TA15 titanium alloy during tensile deformation, J. Mater. Sci. Technol. 98 (2022) 72–86.
[105] Y. Wei, L. Anand, Grain-boundary sliding and separation in polycrystalline metals: application to nanocrystalline fcc metals, J. Mech. Phys. Solids 52 (11) (2004) 2587–2616.
[106] M. Herbig, D. Raabe, Y.J. Li, P. Choi, S. Zaefferer, S. Goto, Atomic-scale quantification of grain boundary segregation in nanocrystalline material, Phys. Rev. Lett. 112 (12) (2014) 126103.
[107] M. Alkayyali, M. Taghizadeh, F. Abdeljawad, Understanding grain boundary segregation and solute drag using computational and machine learning studies, Acta Mater. 275 (2024) 120037.